Electronic Supplementary Material (ESI) for Energy & Environmental Science.
This journal is © The Royal Society of Chemistry 2021

Anionic Redox Induced Anomalous Structural Transition in Ni-rich Cathodes

Jue Liu,[a,#,*] Zhijia Du,[b, #] Xuelong Wang[c], Sha Tan[c,d], Xianyang Wu,[a,e] Linxiao Geng,[b] Bohang Song,[a] Po-Hsiu Chien,[a] S. Michelle Everett,[a] Enyuan Hu[c]

[a] Neutron Scattering Division, Oak Ridge National Laboratory, Oak Ridge, TN 37831, USA

[b] Electrification and Energy Infrastructures Division, Oak Ridge National Laboratory, Oak Ridge, TN 37831, USA

[c] Chemistry Division, Brookhaven National Laboratory, Upton, NY 11973, USA

[d] Department of Chemistry, Stony Brook University, Stony Brook, NY 11974, USA

[e] School of Mechanical Engineering, Purdue University, West Lafayette, IN 47907, USA

S1. Structure evolution of graphite during initial cycle

Reversible phase transitions have been observed for graphite anode during the initial cycle for all four cells (Figures 2 and S6-S9). A close inspection of the enlarged regions reveals relatively complex phase transitions of graphite during lithium intercalation and de-intercalation. The 114 reflection (*d* ~ 1.04 Å, Figure 2) of graphite (S.G. $P6_3$mm) gradually shifts to large d-spacing upon lithiation. Furthermore, there is no detectable formation of new Bragg diffraction peaks, indicating that the initial Li^+ interaction (up to $Li_{\sim0.1}C_6$) follows a solid solution reaction path. This is consistent with previous observations from *in situ* XRD.[1-2] Further lithium insertion leads to the split of the 114 reflection (Figure 2) and the intensity of the new Bragg reflection (at larger *d*-spacing) increases at the expense of the original 114 reflection. In addition, a new and broad diffraction peak emerges at *d*-spacing around1.5 Å (highlighted in dotted blue box in Figure 2). This reflection cannot be indexed using the original graphite phase (S.G. $P6_3$mm, ABAB… stacking of graphene layers) and it continuously shifts toward large d-spacing during further lithiation, indicating it is a solid solution phase instead of a line phase.[2-3] This new phase can be fitted using the lithium intercalated stage III phase (S.G. *P*3 with A(Li)ABA… stacking) only when the intensity of this diffraction peak reaches its maximum (with about 0.15 Li^+ intercalation), as can be seen in Figures 2 and S6-S9. When more than 0.2 Li^+ ($Li_{\sim0.2}C_6$) are inserted into the graphite, a new line phase starts to emerge. The positions of corresponding diffraction peaks remain almost unchanged, as can be seen in Figure 2. A close inspection of the diffraction peak around 1.23 Å (110 reflection of graphite) shows a small peak splitting when 0.25 to 0.5 Li^+ were inserted (Figure S2c), indicating the co-existence of two distinct phases within this region. The difference between these two phases is likely caused by the in *ab*-plane lithium-vacancy arrangements since the average interlayer spacing remains almost identical. This observation is fully consistent with the previous reports of the diluted stage-II phase (LiC_{18} with AB(Li)BA…stacking) to stage-II phase (LiC_{12}, S.G. *P*6mm with AA(Li)AA…stacking) transition in this region.[1] Further lithium insertion leads to the phase transition from the stage II phase to the fully lithiated stage I phase (LiC_6, S.G. *P*6mm with A(Li)A… stacking).

S2. The relationship between the bond lengths evolution and lattice parameter evolution

In the classic O3-type $LiTMO_2$ structure (S.G. *R*-3m), the only refinable atomic coordination is the *z*-coordinate of oxygen (O_z), and the average Li-O, TM-O bond lengths and interlayer O-O distances within TMO_2 slab can be calculated using equations S1-S3. The average Li-O/TM-O bond distance and interlayer O-O distances are correlated with both lattice parameters and O_z. Thus, the evolution of lattice parameters or cell volume alone may not truly reflect the average structure change. As shown in Figure S50, the refined O_z of four samples steadily decrease towards 74% - 76% delithiation. Recall that *c*-lattice starts to collapse while a remains almost unchanged at SOCs above 67%. The bond lengths (or distances) of Li-O, TM-O and interlayer O-O depend on the relative (and opposite) contributions from c-lattice and O_z. Considering that O_z are refined to be somewhere between 0.22 and 0.24, and ($1/3-O_z$) is larger than ($O_z-1/6$), the change of average Li-O bond lengths is predominantly affected by the change of lattice parameter c while TM-O bond lengths and interlayer O-O distances are expected to be dominated by the variation of O_z. This explains why the turning point (at SOC of 74 - 76%) for TM-O bond lengths and interlayer O-O distances match very well with that of the O_z. Similar behavior has also been observed for the evolution of O-TM-O bond angles (Figure S44) and TMO_2 slab thickness (Figure 5). In contrast, the change of Li-O bond lengths and LiO_2 slab thickness are dictated by the change of lattice parameter *c*, leading to a more consistent trends between these parameters (Figures 4-5). The structural change is in large part reversible during the initial discharge (to 2.8 V versus graphite), despite the existence of small hysteresis for most compositions. This reversible structure change during the initial charge and discharge suggests that the bulk structure is well maintained without obvious structure decomposition even charged to very high SOCs (e.g., ~90% in NMC811).

S3. Electronic structures of $LiNiO_2$ and Ni-rich NMC/NCA cathodes.

The ground state structure and electronic structure of $LiNiO_2$ is still of great controversies.[4-8] The lack of both cooperative Jahn-Teller ordering and low temperature magnetic ordering in a compound with low-spin JT active Ni^{3+} have attracted tremendous attentions from both experimental and theoretical communities in the last few decades.[6, 9-14] A few ground state structure models have been proposed to explain these abnormal behaviors, including the short-range JT model with randomly oriented JT orbitals (d_{z^2}) or nanometer ordered domains,[8, 12, 15] charge disproportionation[16], and the more recently proposed dynamical mixture or high entropy electronic configurations.[13, 17] Despite these great controversies, a somewhat unified electronic structure picture has been reported, as can be seen from the schematic form of density of state (DOS) shown in Figure S53. Although there are different interpretations of the small band gap (measure band gap of 0.4–0.5 eV),[18] it is generally agreed the two split bands around the Fermi level are strongly correlated with the strong *p-d* hybridization between Ni and O.[6, 13, 17] In addition, these split states are of predominant Ni *3d* feature with e_g symmetry ($d_{x^2-y^2}$ and d_{z^2}), as confirmed by XAS studies where Ni K-edge spectra shift to higher energy during lithium removal at relatively low SOCs (< 70%).[19-21] More complicated DOSs are expected for Ni-rich NMCs or NCAs as these compounds contain multiple TM cations in different oxidation states. For instance, Ni^{2+}, Ni^{3+}, Co^{3+} and Mn^{4+} co-exist in NMCs while Ni^{3+}

and Co^{3+} coexist in NCA. Since the hybridized *3d*-states of Mn^{4+} locate at energies well above or below the Fermi energy (Figure S54), they are unlikely to directly contribute to the charge compensation (though the strong electron localization effect associated with Mn^{4+} may affect the charge/discharge potentials).[22] We will thus omit the contribution from Mn^{4+} in the schematic DOS (Figure 7) for clarity. The position of Ni^{2+} dominated e_g* states (spin up) locates slightly above the filled Ni^{3+} e_g* state since it has been confirmed that the Ni^{2+}/Ni^{3+} redox takes place earlier than the Ni^{3+}/Ni^{4+} redox.[21] Therefore, the small band gaps in NMCs and NCAs are between the empty (spin up) Ni^{3+} e_g* state and the filled (spin up) Ni^{2+} e_g* state.[23] The situation of the filled states with predominant Co t_{2g}* feature (hybridized with oxygen *2p*) is still fiercely debated. It used to be believed that Co^{3+} only participates in charge compensation at very high SOCs, suggesting that this state sits below the filled Ni e_g* states and is close to the top of itinerant oxygen *2p* band (Figure 7).[20-21] However, recent evidences from both XAS and EXAFS show that Co participates in the charge compensation at a much earlier stage (in concomitance with the oxidation of Ni),[24-25] indicating that the predominant Co t_{2g}* featured states may sit very close to the filled Ni e_g* states, as demonstrated in Figure 7. Taken together, this allows us to draw the schematic DOS for Ni-rich NCMs (e.g., NMC811, Figure 7), a qualitative picture that is very close to many recent DFT calculations.[23]

During the initial stage of charge, electrons are first taken from the filled Ni^{2+} e_g* dominant anti-bonding states (σ*), corresponding to the nominal oxidation of Ni^{2+} to Ni^{3+}. This leads to the increase of the DOS of Ni^{3+} e_g* at the expense of Ni^{2+} e_g*, as can be seen in Figure 7. Further lithium removal is accompanied by taking electrons from the filled Ni^{3+} e_g* states and/or Co t_{2g}* dominant states. There are two consequences associated with this process: First, the hybridization between Ni/Co 3d and oxygen *2p* will increase. This leads to the increase of covalency between Ni/Co and ligand oxygen, resulting in the decrease of the effective electron density on ligand oxygen ions. The increased hybridization will also push the antibonding states up and the bonding states down;[26] Second and more importantly, the oxidation of Ni^{3+}/Co^{3+} further decreases the charge transfer gap (ΔCT) of this small charge transfer gapped material (by decreasing the energy level of TM *3d* orbitals (ε_d) relative to the energy level of oxygen *2p* orbitals (ε_p), as can be seen in Figure 7). This effectively pushes the compound into the so-called very small (ΔCT ~0) or negative (ΔCT <0) charge transfer gapped oxides.[27] In this situation, the top part of the broad oxygen *2p* band is of predominant oxygen *2p* t_{2g}* feature. It is expected that with a large decrease of ΔCT, the latter (or second) effect dominates. Therefore, the filled Ni e_g* and partially empty Co t_{2g}* states (admixture with oxygen *2p*) start to overlap with the top part of the itinerant oxygen *2p* band, as demonstrated in Figure 7. Overall, it leads to a very complicated charge compensation mechanism, where electrons can be potentially taken from all three states with drastically different natures. Thus, electron holes may be created on both strongly hybridized Ni/Co *3d* anti-bonding states and itinerant oxygen *2p* dominated t_{2g}* bands. As ΔCT continues decreasing with further Li^+ removal, the empty Ni *3d* e_g* states will eventually overlap with the itinerant oxygen *2p* band (Figure 7). This resembles the situation of moving a transition metal oxides from the positive charge transfer gap region to the negative charge transfer gap region (e.g., by hole doping) in the classical ZSA model.[27-28]

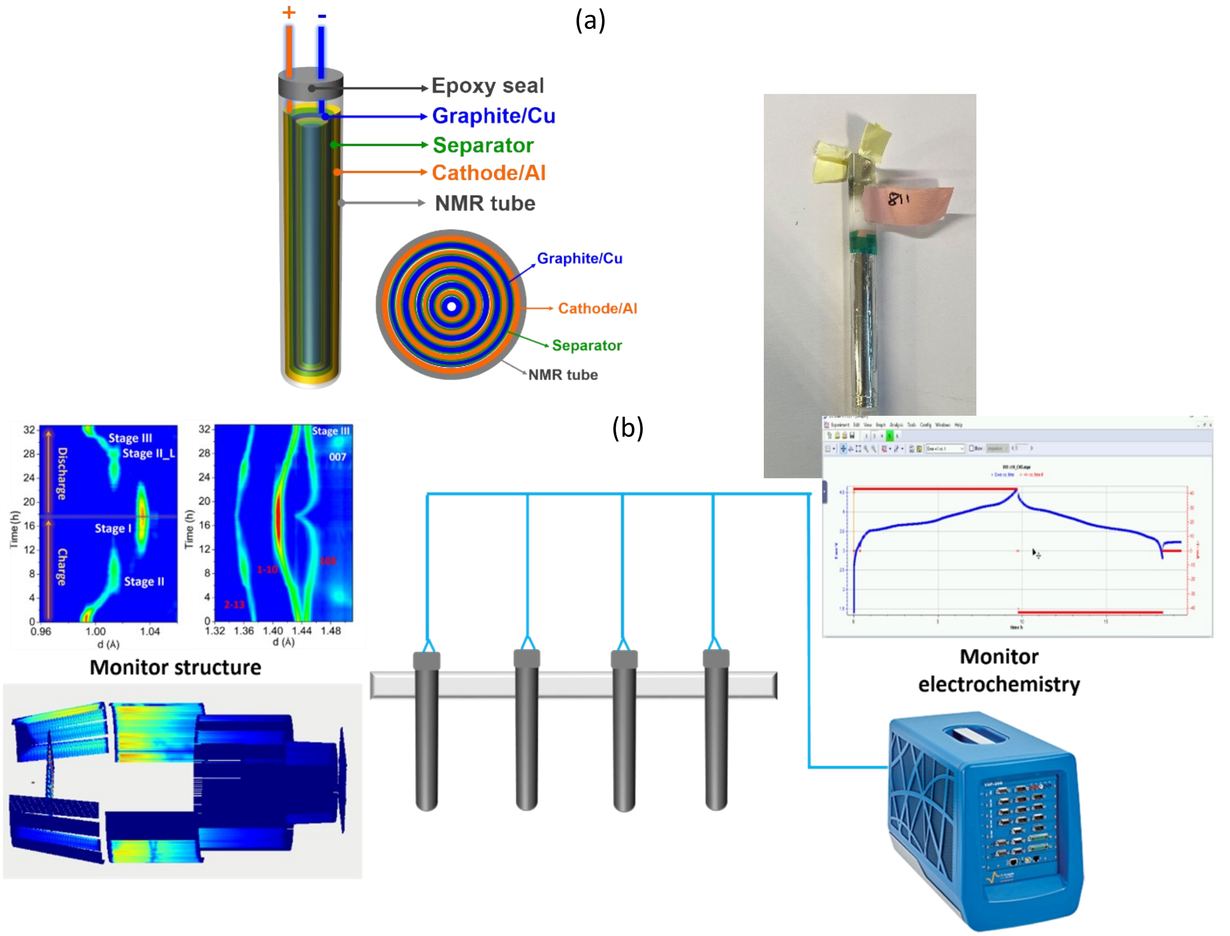

Figure S1. (a) Schematic of the newly designed *in situ* neutron diffraction cell with a real cell displayed on the right. (b) Schematic of four *in situ* cells on the shift bracket for high throughput *operando* neutron diffraction measurements.

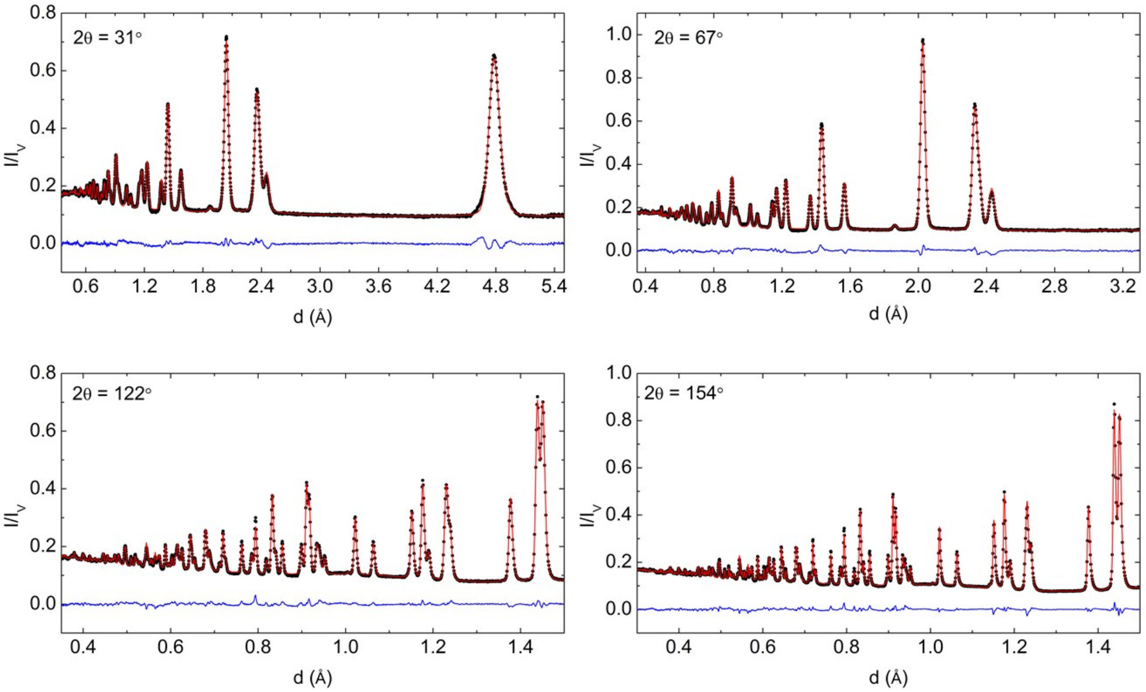

Figure S2. Rietveld refinement of the structure of pristine NMC532.

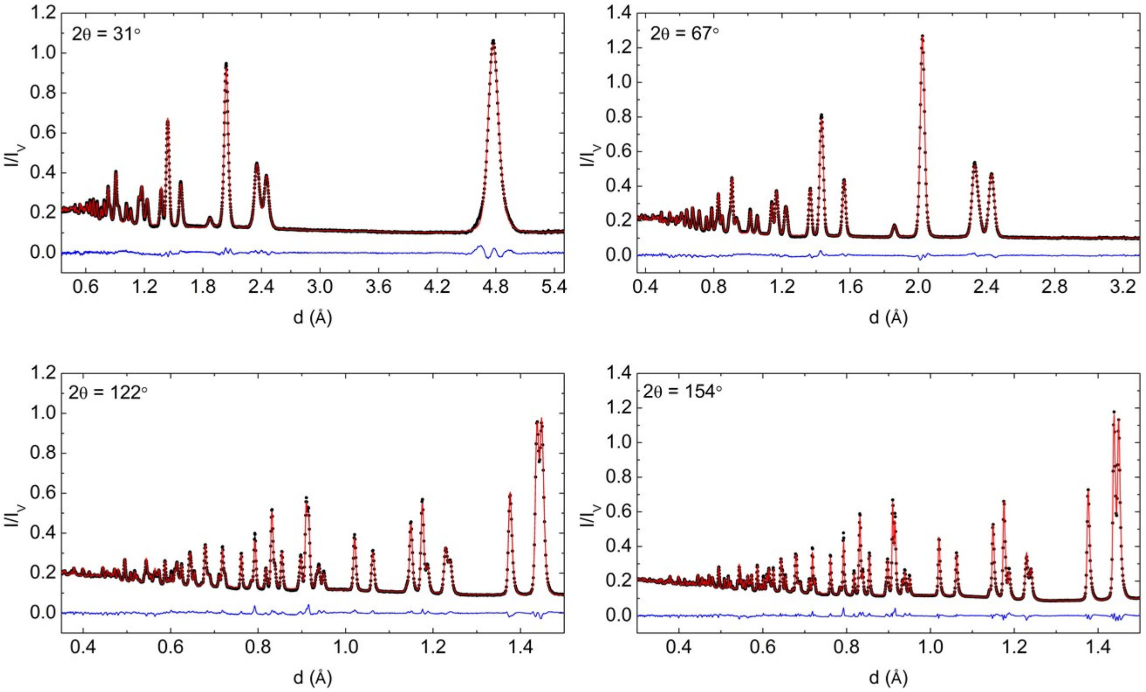

Figure S3. Rietveld refinement of the structure of pristine NMC622.

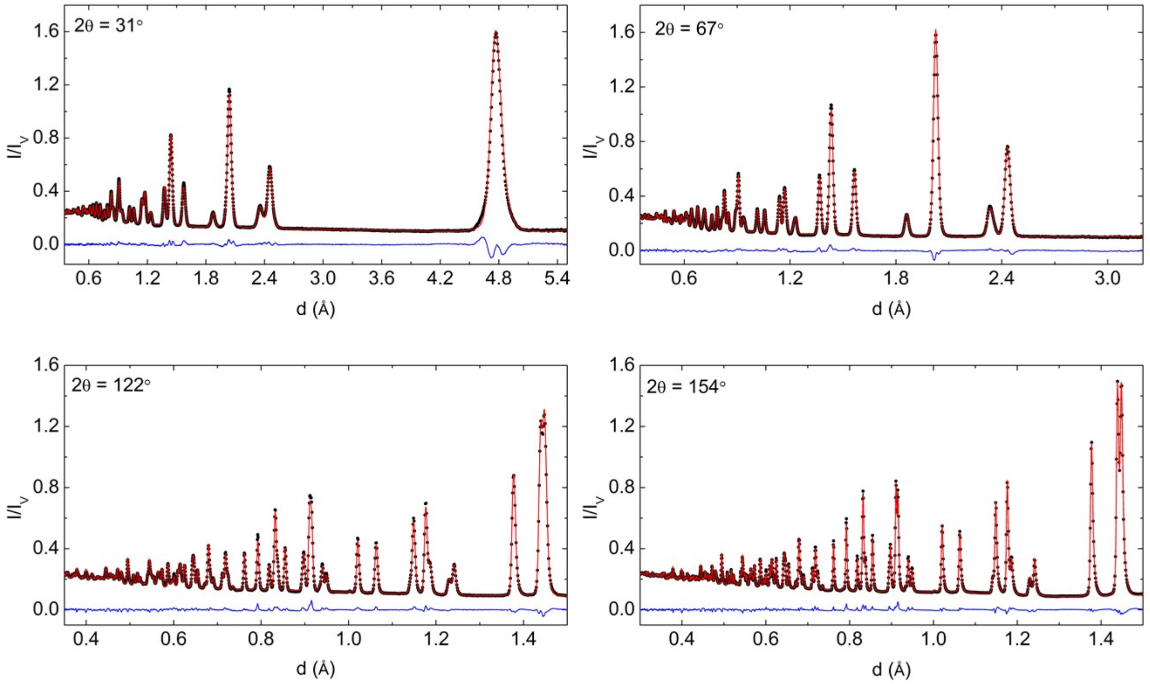

Figure S4. Rietveld refinement of the structure of pristine NMC811.

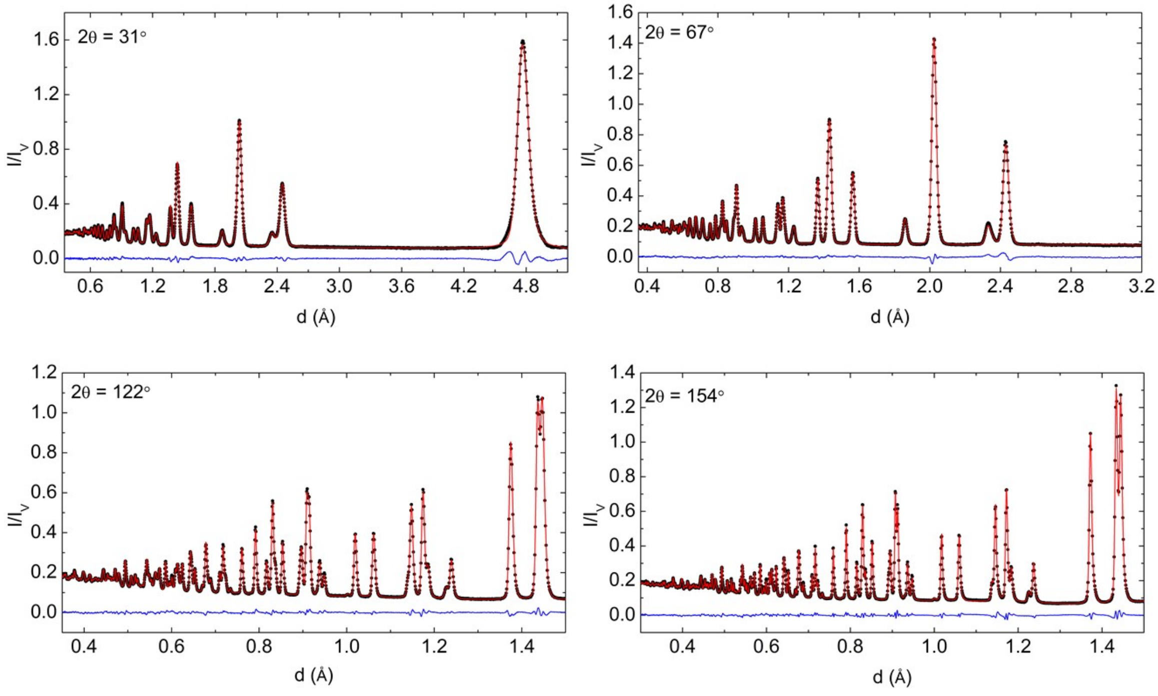

Figure S5. Rietveld refinement of the structure of pristine NCA.

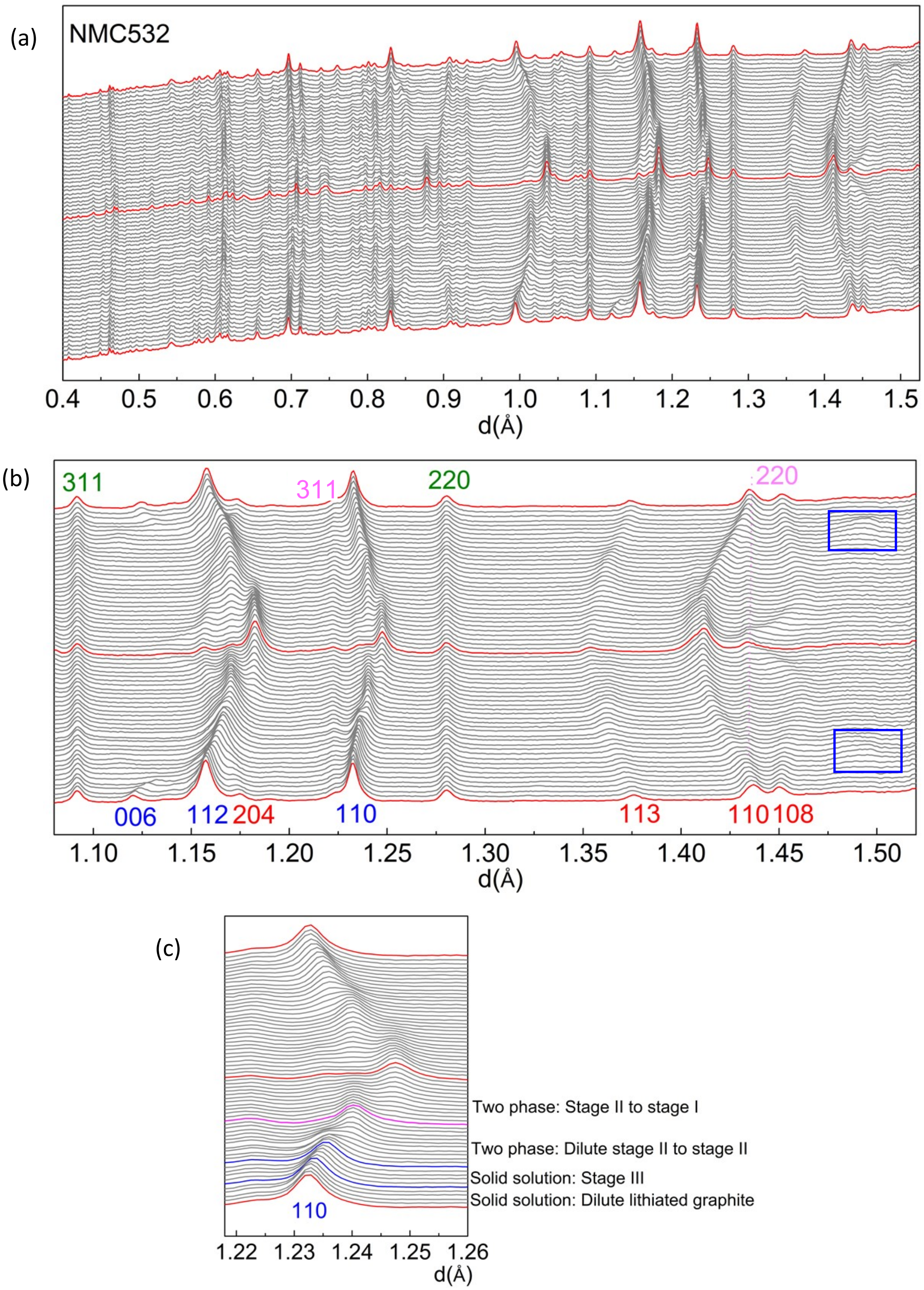

Figure S6. (a) *In situ* neutron diffraction data (high resolution bank, center $2\theta = 154°$) of NMC532 (against graphite anode) collected during the initial charge and discharge. (b) Enlarged region (1.08 – 1.52 Å) with major Bragg reflections of NMC532, graphite (lithiated graphite), Cu and Al (highlighted in dotted line) labeled in red, blue, olive and magenta respectively. The 007 reflection of stage III phase of the lithiated graphite is highlighted in dotted blue box. It can be seen that this broad diffraction peak continuously shifts toward the small d-spacing during lithiation and it moves to the opposite direction during delithiation, indicating it is a solid solution phase instead of a line phase. (c) The enlarged region of graphite 110 reflection showing the evolution of different staging phases of graphite during lithiation.

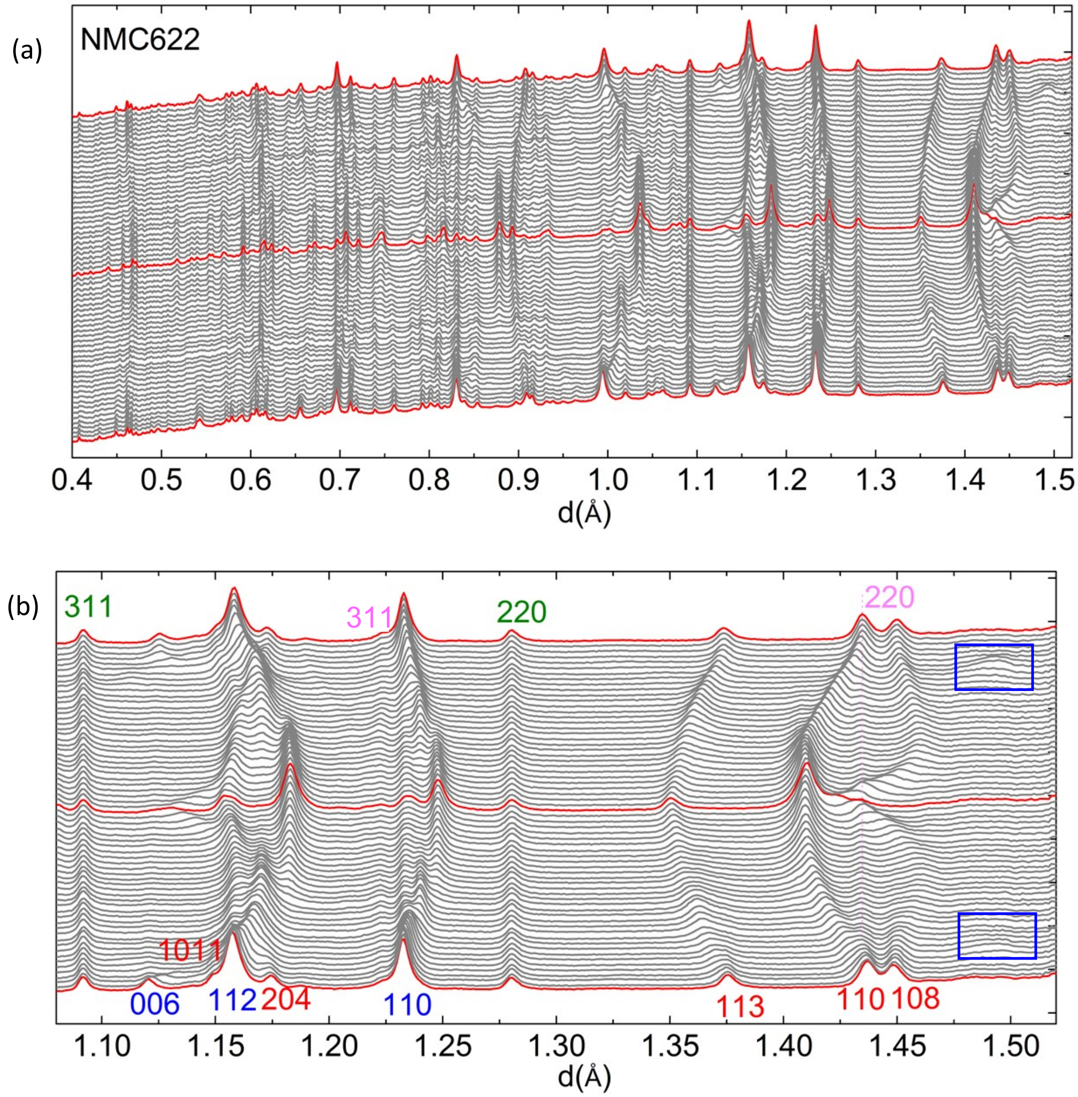

Figure S7. (a) *In situ* neutron diffraction data (high resolution bank, center $2\theta = 154°$) of NMC622 (against graphite anode) collected during the initial charge and discharge. (b) Enlarged region (1.08 – 1.52 Å) with major Bragg reflections of NM6222, graphite (lithiated graphite), Cu and Al (highlighted in dotted line) labeled in red, blue, olive and magenta. It is worth noting that there are extra amounts of graphite in the NMC622 cell because of the double layer coating, i.e., the last layer of graphite does not have corresponding counter cathode electrode. Therefore, diffraction peaks of residual graphite can be seen through the entire charge/discharge cycle.

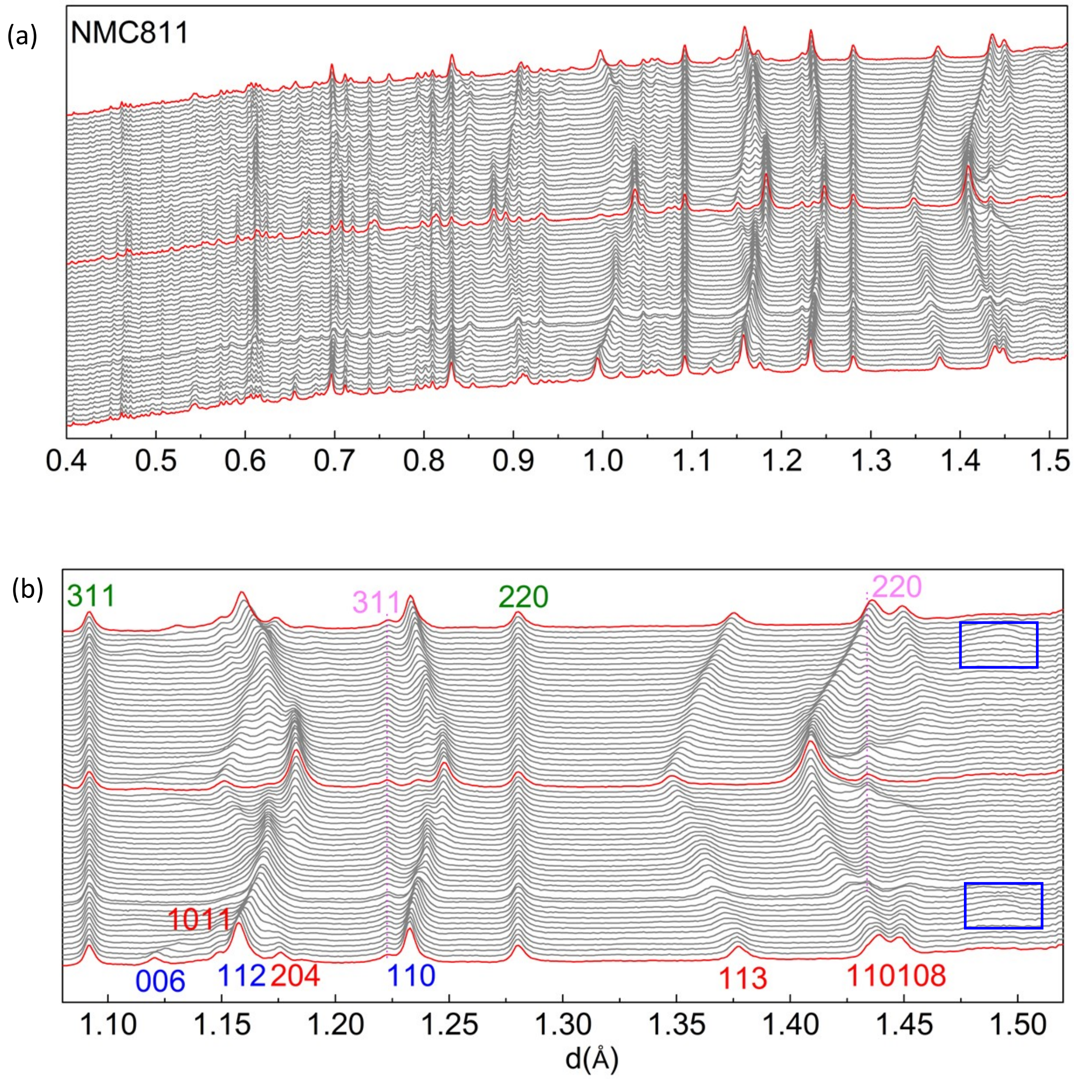

Figure S8. (a) *In situ* neutron diffraction data (high resolution bank, center $2\theta = 154°$) of NMC811 (against graphite) collected during the initial charge and discharge. (b) Enlarged region (1.08 – 1.52 Å) with major Bragg reflections of NMC811, graphite (lithiated graphite), Cu and Al (highlighted in dotted line) labeled in red, blue, olive and magenta.

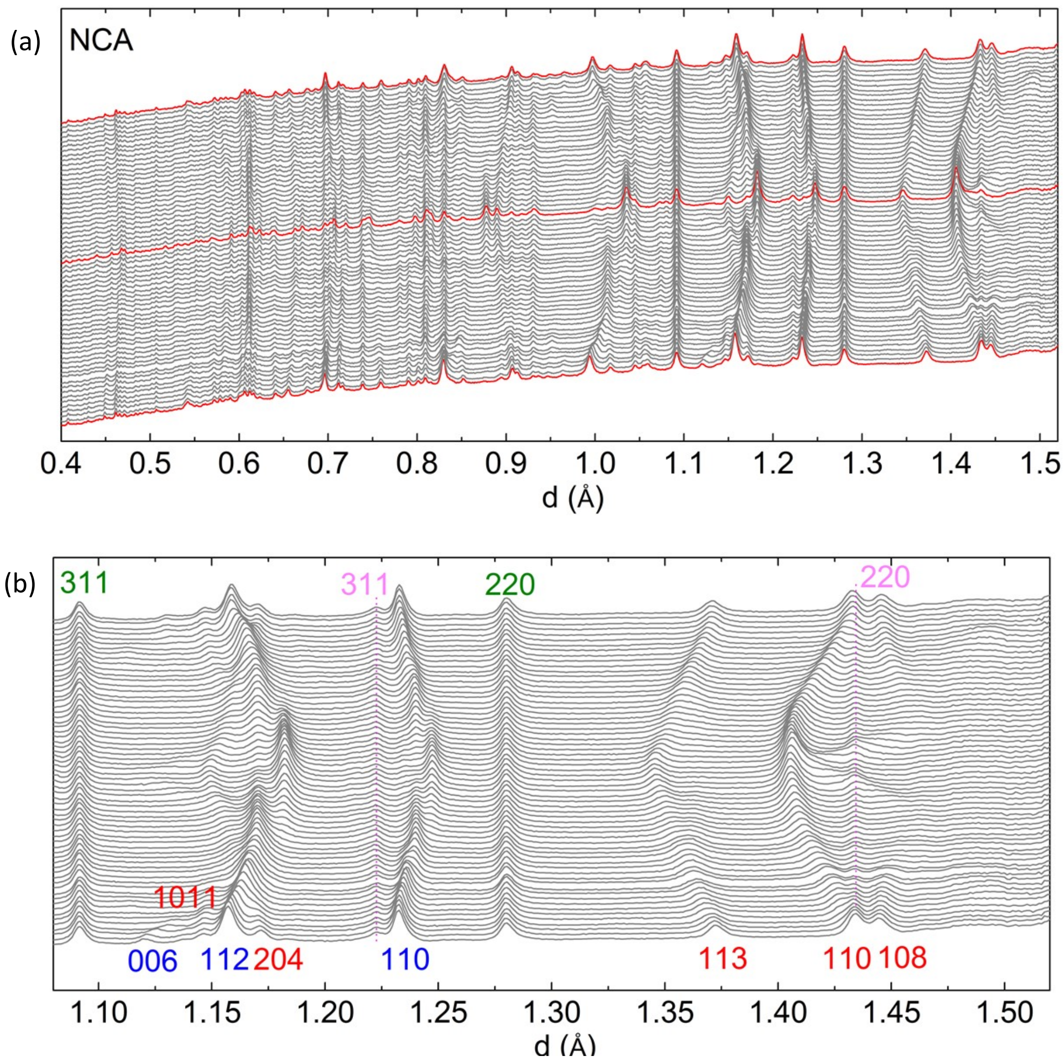

Figure S9. (a) *In situ* neutron diffraction data (high resolution bank, center 2θ = 154°) of NCA (against graphite) collected during the first cycle. (b) Enlarged region (1.08 – 1.52 Å) with major Bragg reflections of NCA, graphite (lithiated graphite), Cu and Al (highlighted in dotted line) labeled in red, blue, olive and magenta respectively.

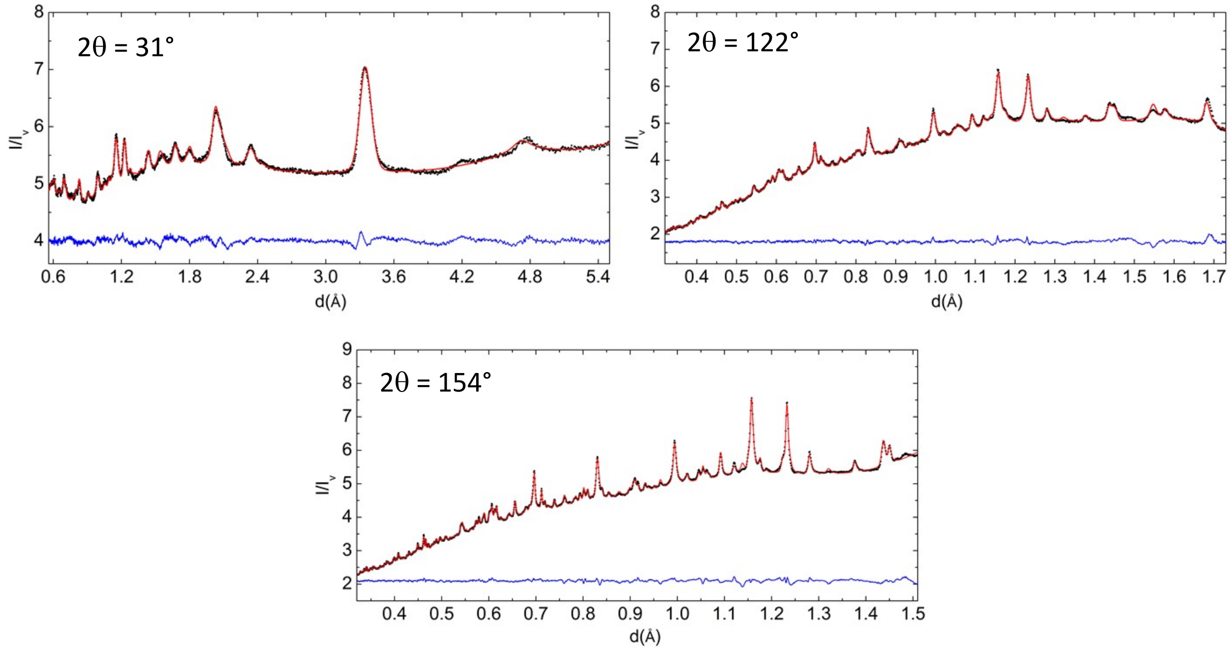

Figure S10. Rietveld refinement of structures of pristine NMC532, graphite, Cu and Al using *in situ* neutron diffraction data (three frames data) collected before charging.

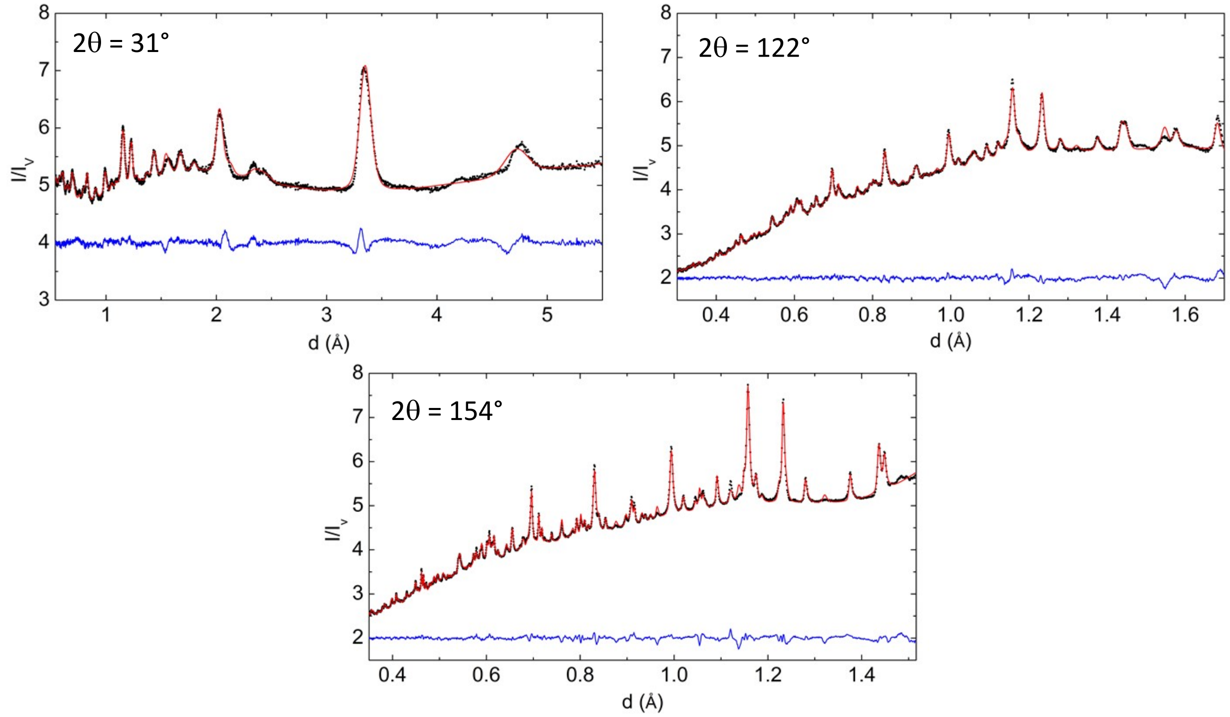

Figure S11. Rietveld refinement of structures of pristine NMC622, graphite, Cu and Al using *in situ* neutron diffraction data (three frames data) collected before charging.

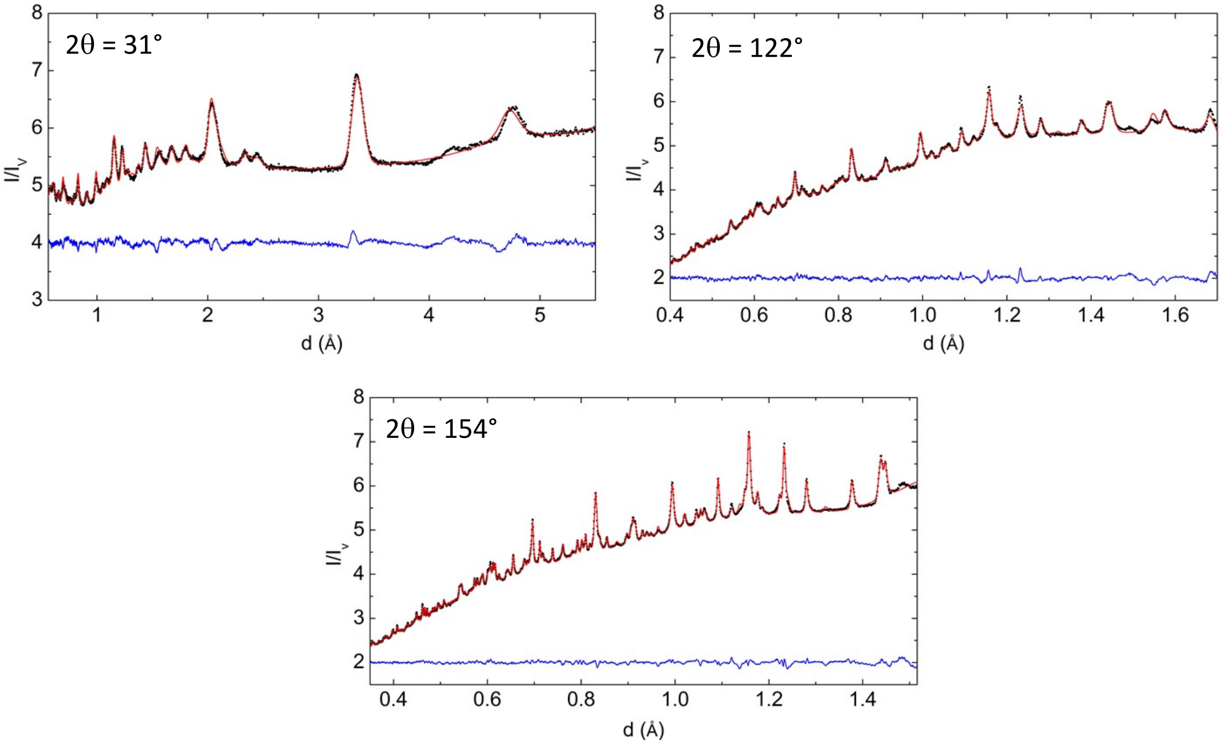

Figure S12. Rietveld refinement of structures of pristine NMC811, graphite, Cu and Al using *in situ* neutron diffraction data (three frames data) collected before charging.

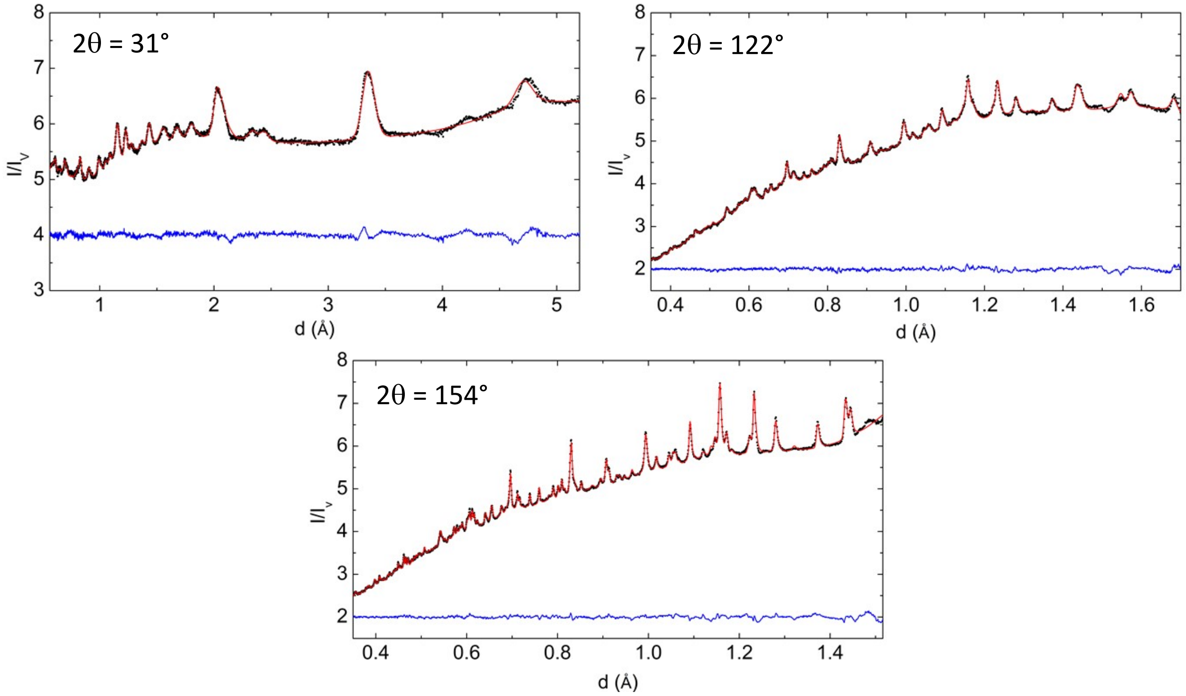

Figure S13. Rietveld refinement of structures of pristine NCA, graphite, Cu and Al using *in situ* neutron diffraction data (three frames data) collected before charging.

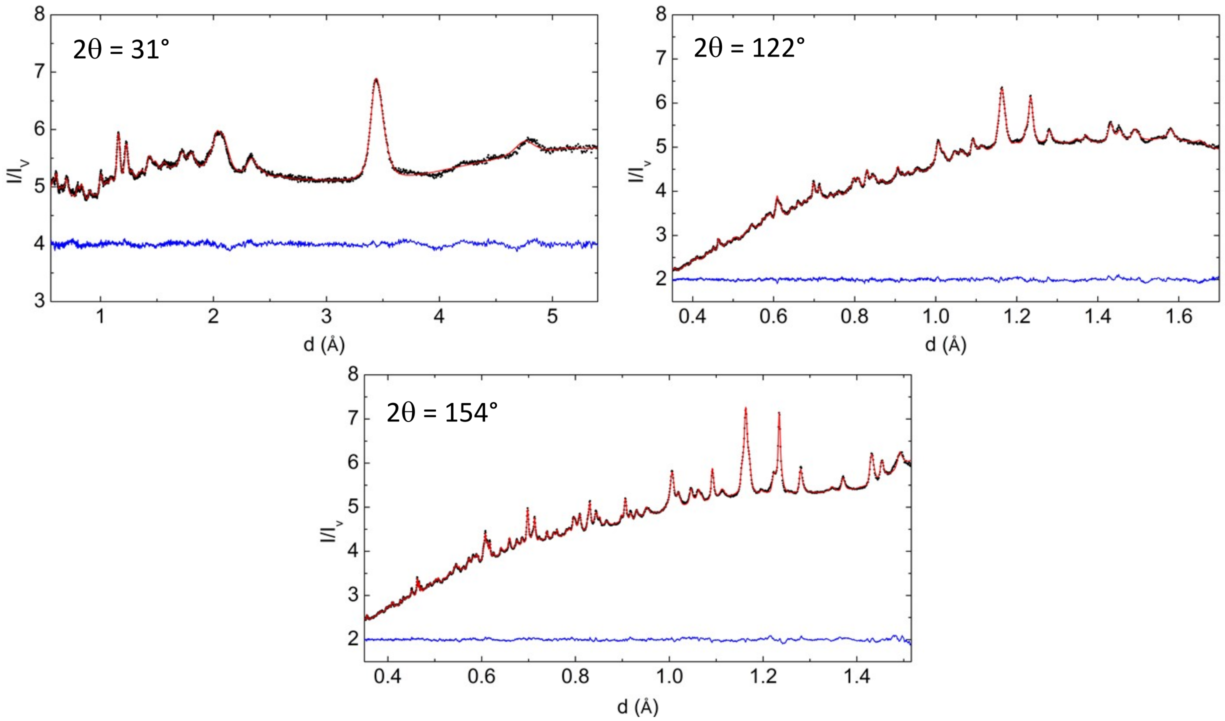

Figure S14. Rietveld refinement of structures of charged NMC532 (15%), lithiated graphite (at stage III), Cu and Al using *in situ* neutron diffraction data.

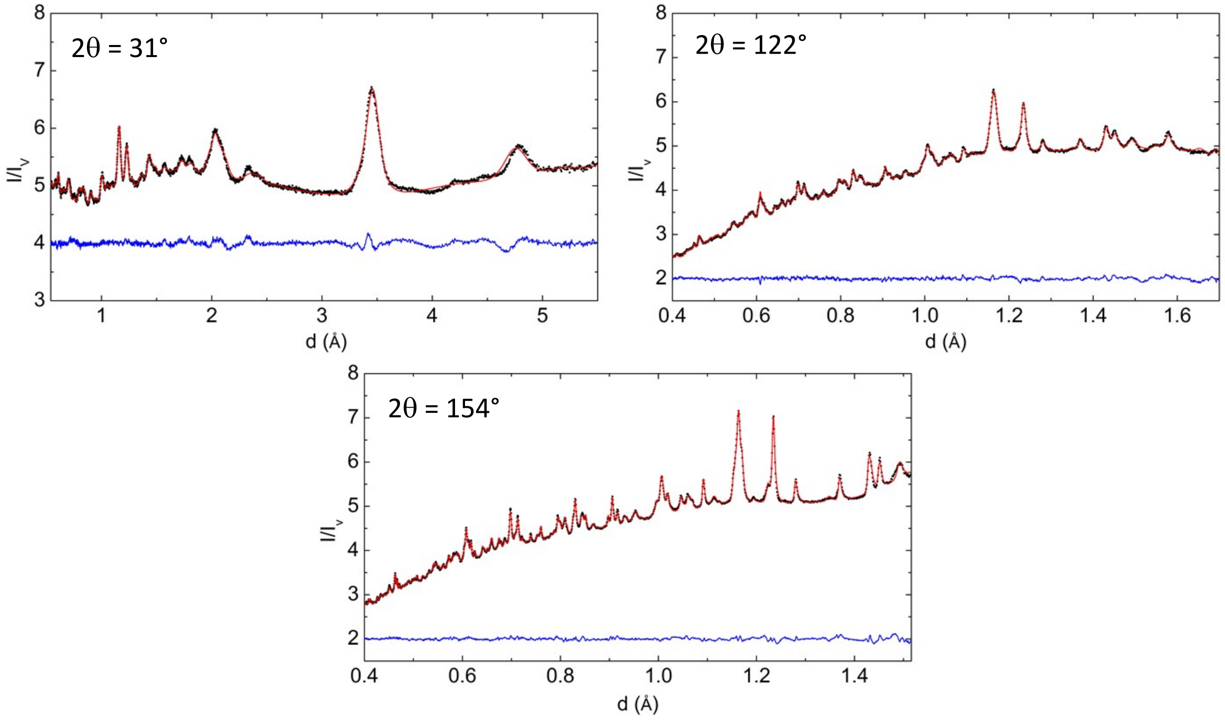

Figure S15. Rietveld refinement of structures of charged NMC622 (15%) , lithiated graphite (at stage III), Cu and Al using *in situ* neutron diffraction data.

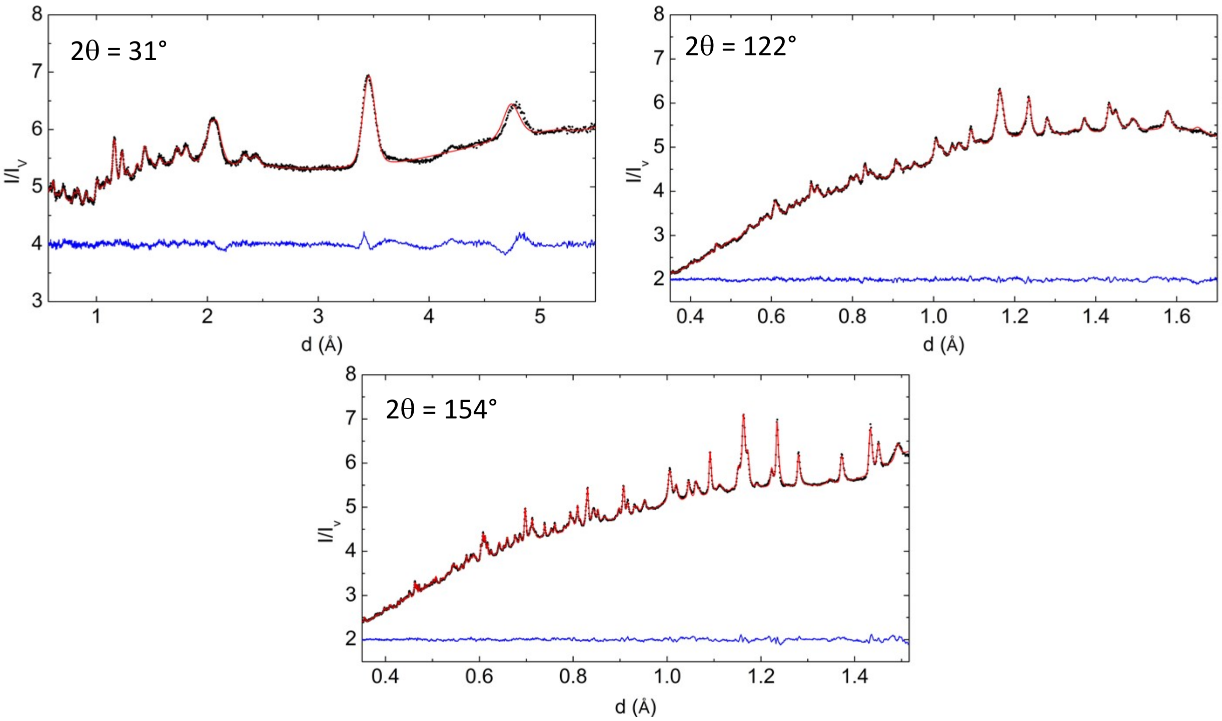

Figure S16. Rietveld refinement of structures of charged NMC8111 (15%), lithiated graphite (at stage III), Cu and Al using in situ neutron diffraction data.

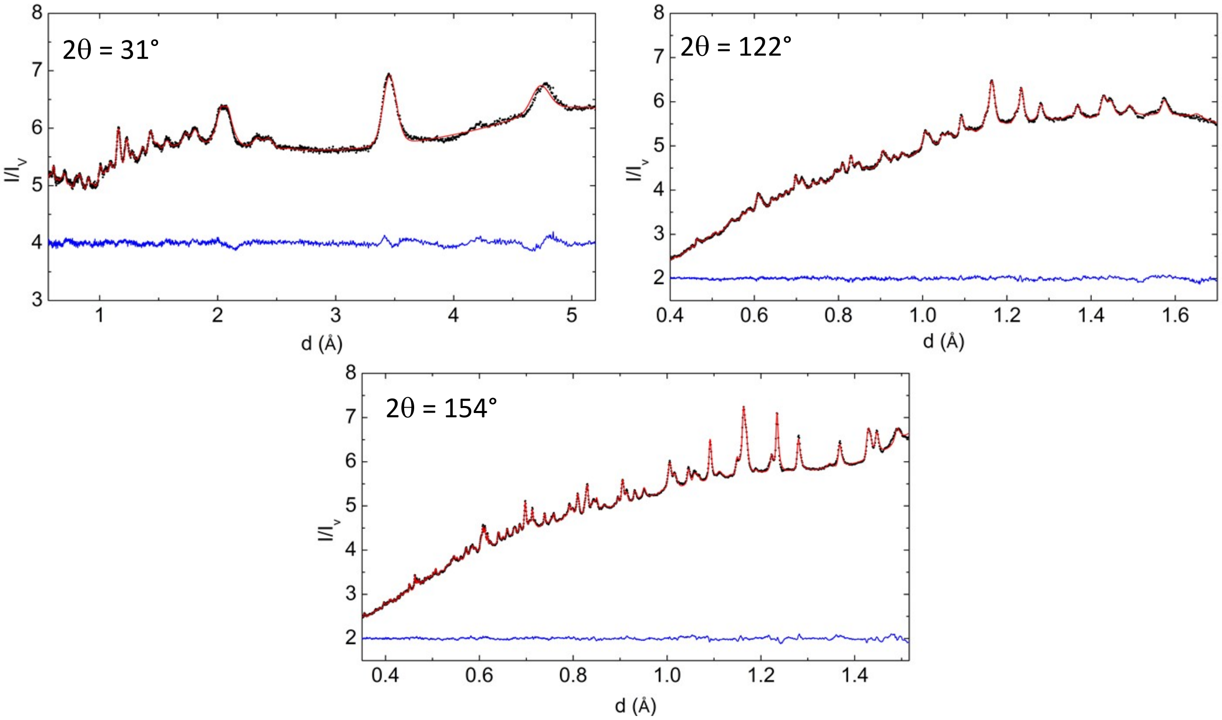

Figure S17. Rietveld refinement of structures of charged NCA (15%), lithiated graphite (at stage III), Cu and Al using in situ neutron diffraction data.

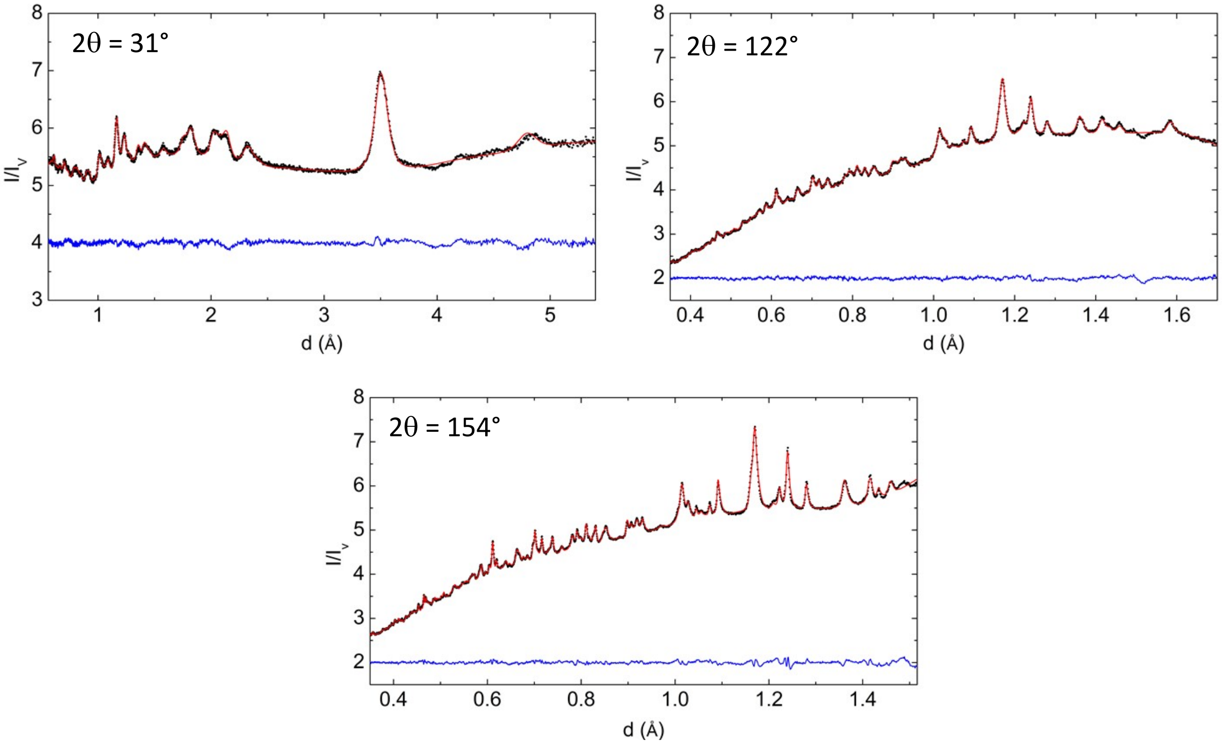

Figure S18. Rietveld refinement of structures of charged NMC532 (46%), lithiated graphite (at stage II), Cu and Al using *in situ* neutron diffraction data.

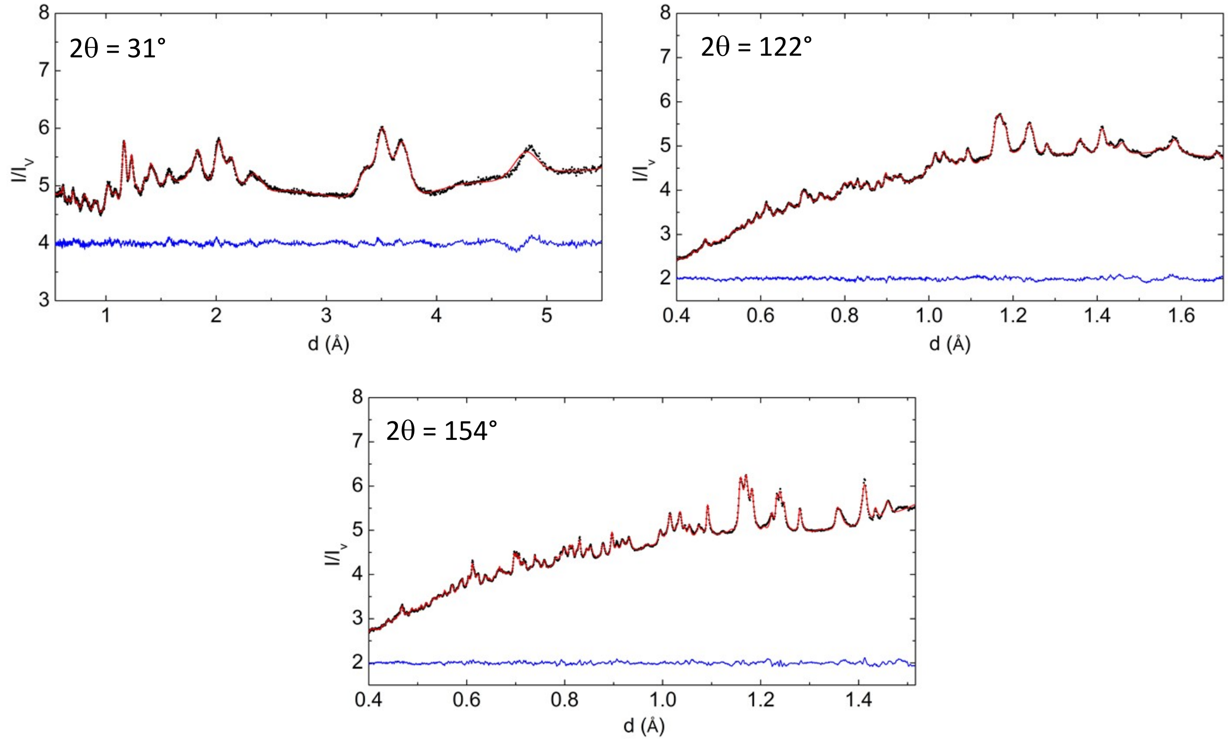

Figure S19. Rietveld refinement of structures of charged NMC622 (46%), lithiated graphite (at stage III), Cu and Al using *in situ* neutron diffraction data.

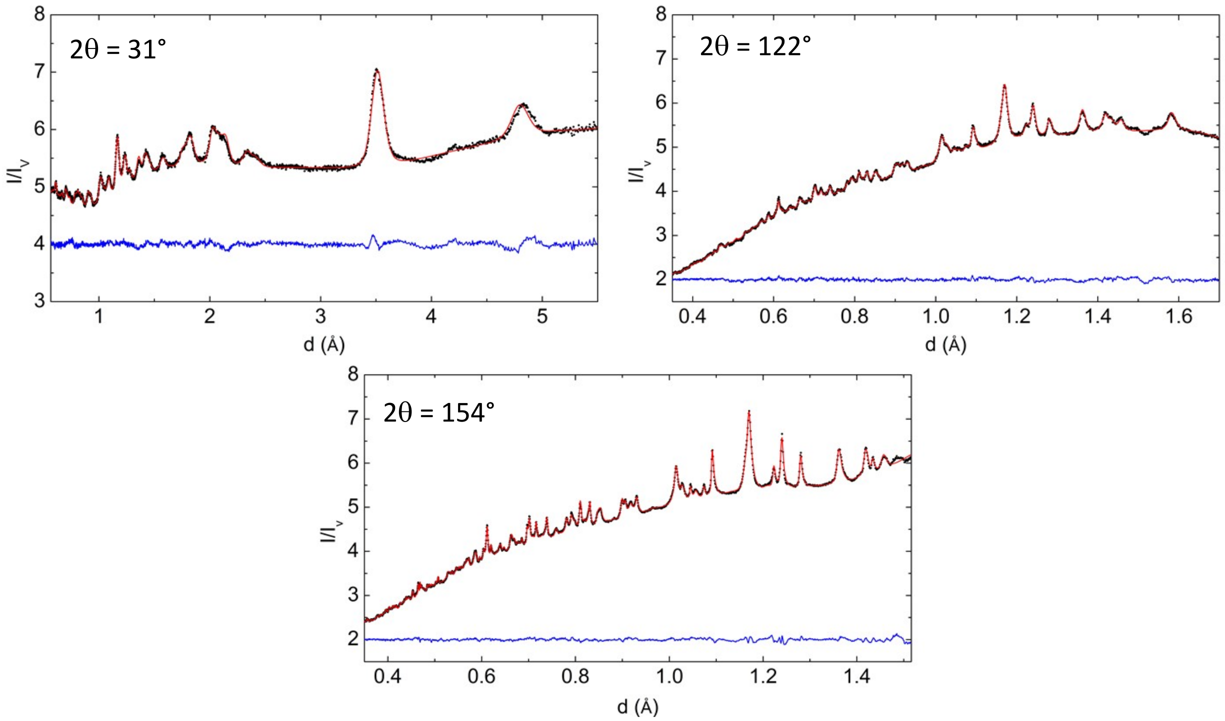

Figure S20. Rietveld refinement of structures of charged NMC811 (46%), lithiated graphite (at stage II and stage I), Cu and Al using *in situ* neutron diffraction data.

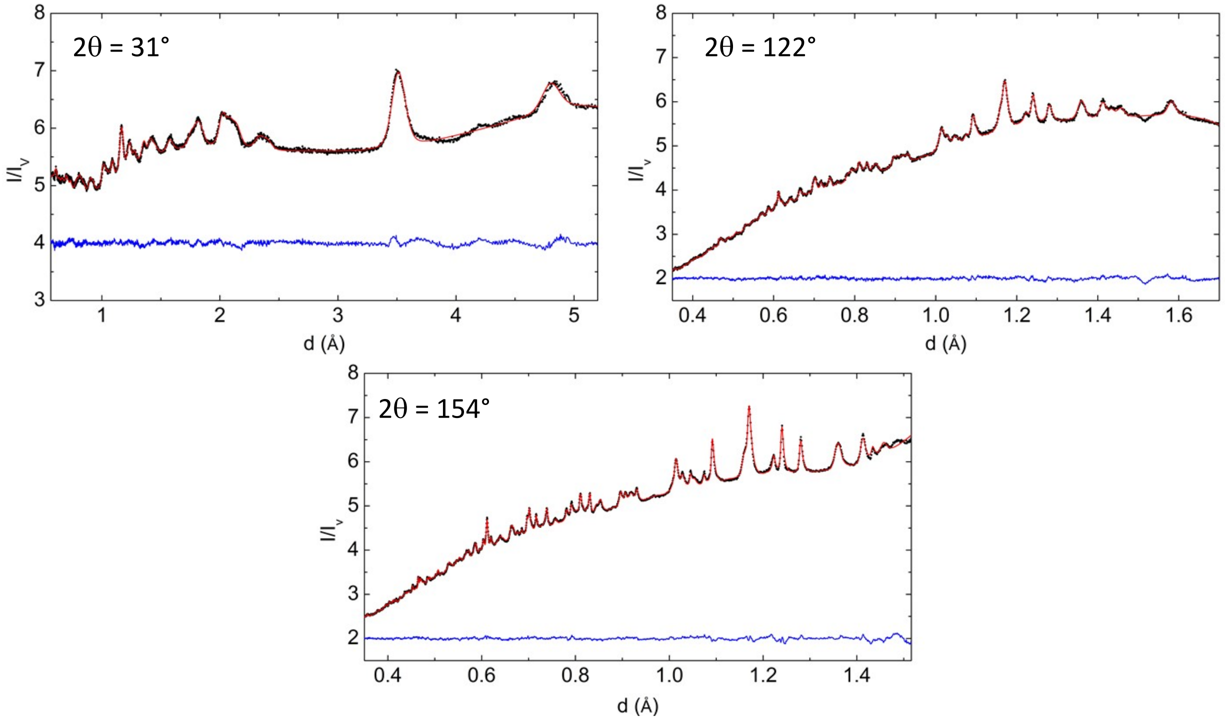

Figure S21. Rietveld refinement of structures of charged NCA (46%), lithiated graphite (at stage II and stage I), Cu and Al using *in situ* neutron diffraction data.

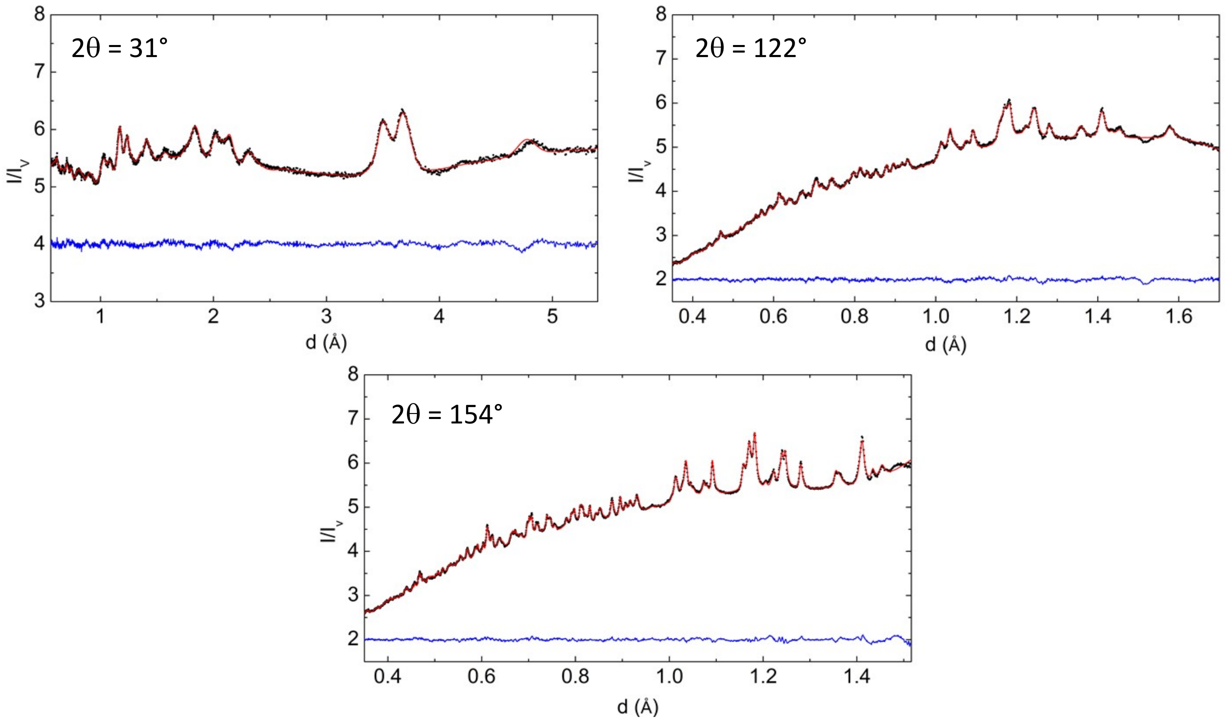

Figure S22. Rietveld refinement of structures of charged NMC532 (67%), lithiated graphite (at stage II + stage I), Cu and Al using *in situ* neutron diffraction data.

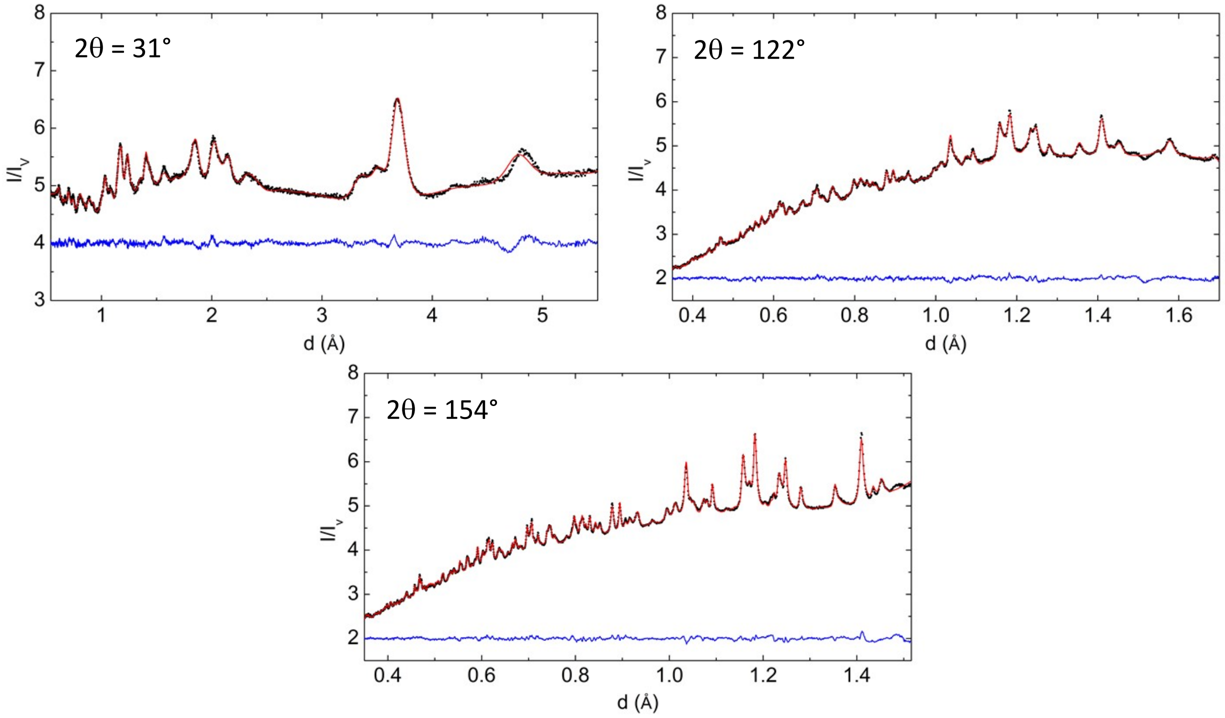

Figure S23. Rietveld refinement of structures of charged NMC622 (67%), lithiated graphite (at stage III), Cu and Al using *in situ* neutron diffraction data.

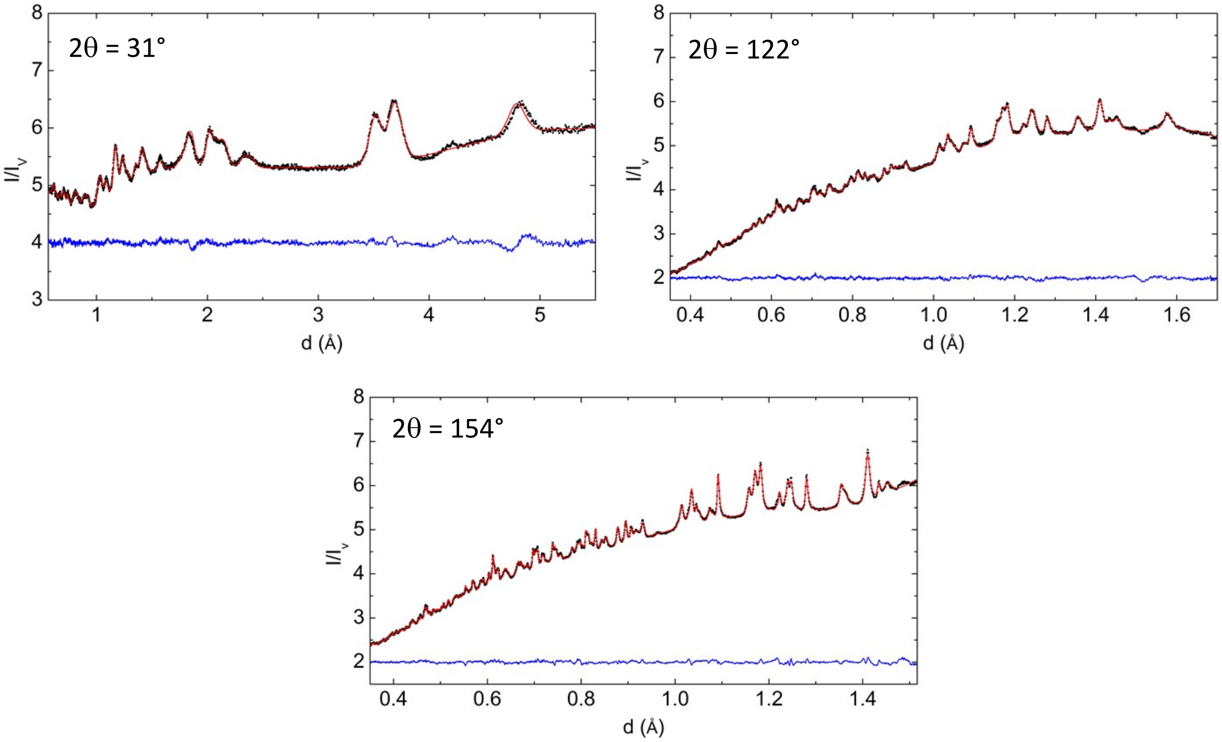

Figure S24. Rietveld refinement of structures of charged NMC811 (67%), lithiated graphite (at stage II and stage I), Cu and Al using *in situ* neutron diffraction data.

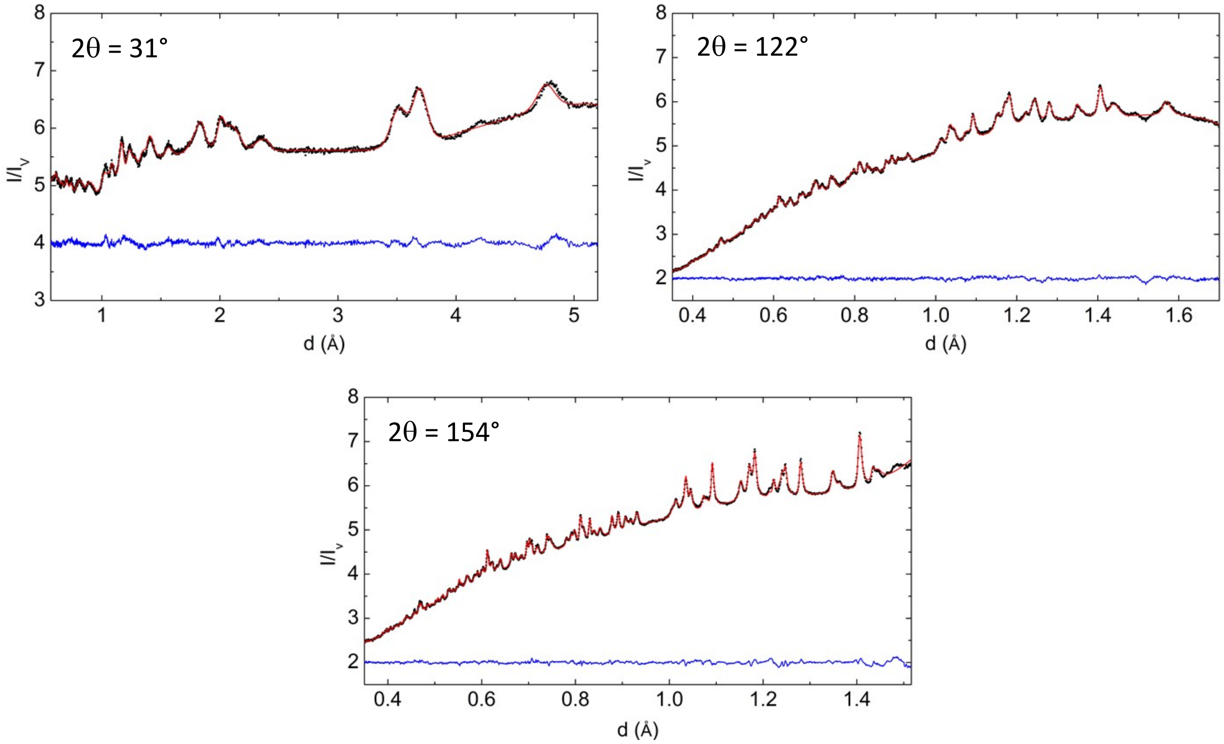

Figure S25. Rietveld refinement of structures of charged NCA (67%), lithiated graphite (at stage II and stage I), Cu and Al using *in situ* neutron diffraction data.

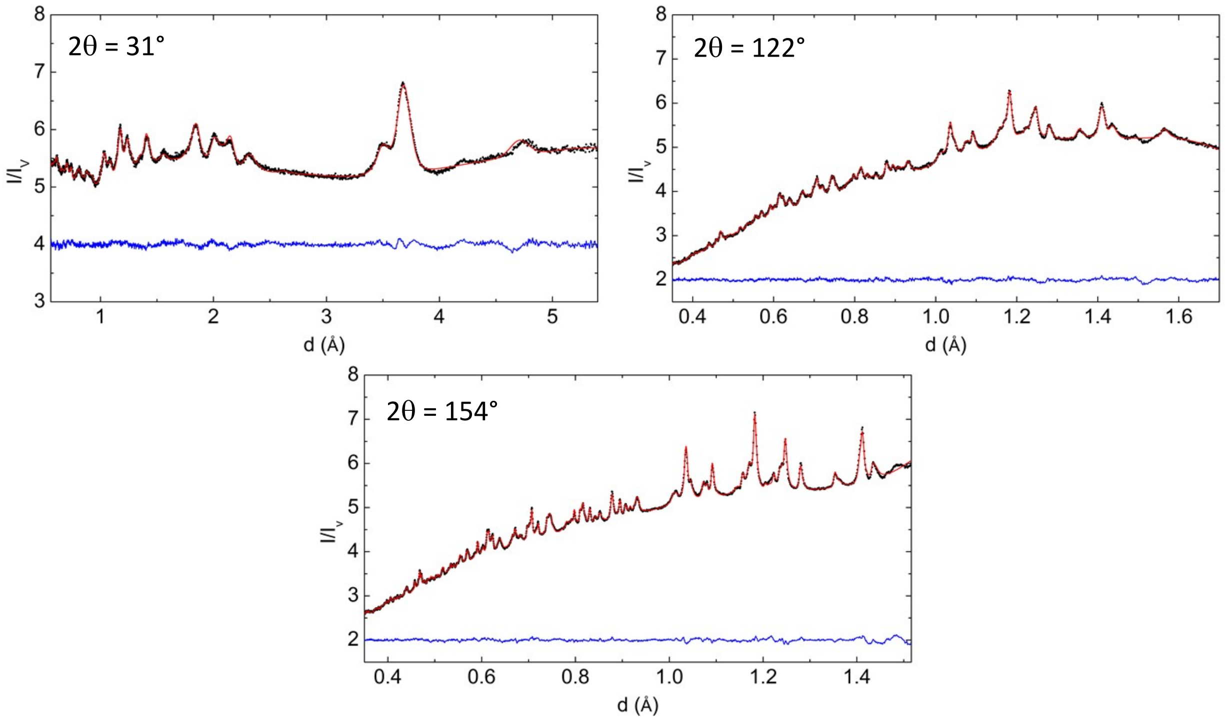

Figure S26. Rietveld refinement of structures of charged NMC532 (75%), lithiated graphite (at stage II + stage I), Cu and Al using *in situ* neutron diffraction data.

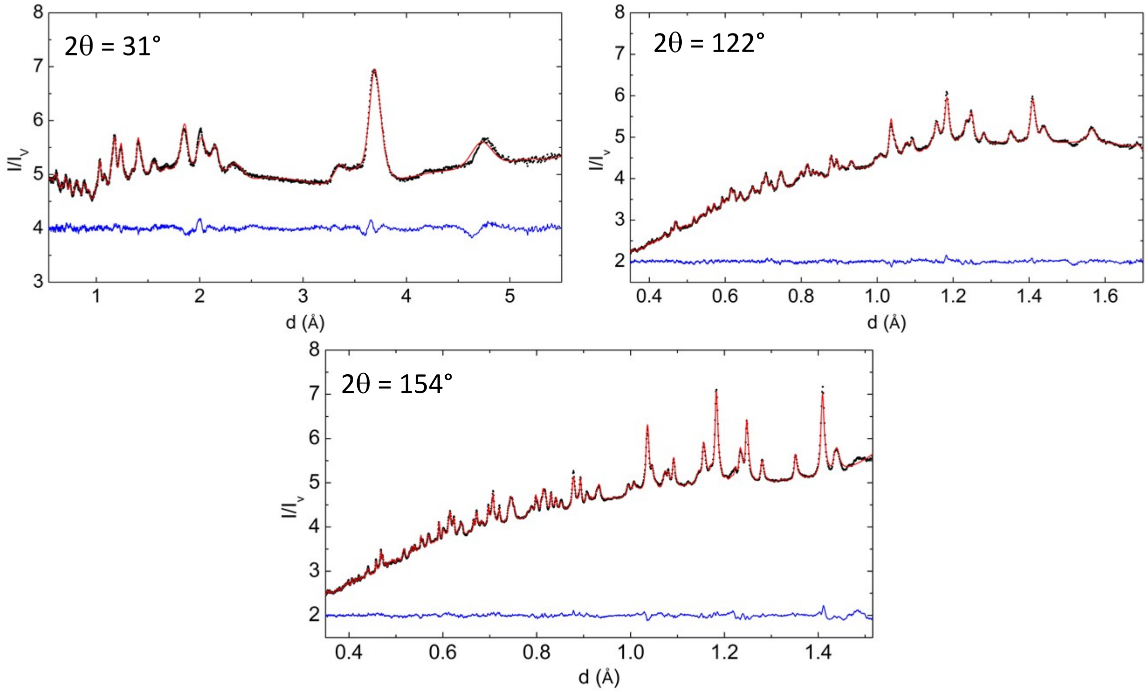

Figure S27. Rietveld refinement of structures of charged NMC622 (75%), lithiated graphite (at stage III), Cu and Al using *in situ* neutron diffraction data.

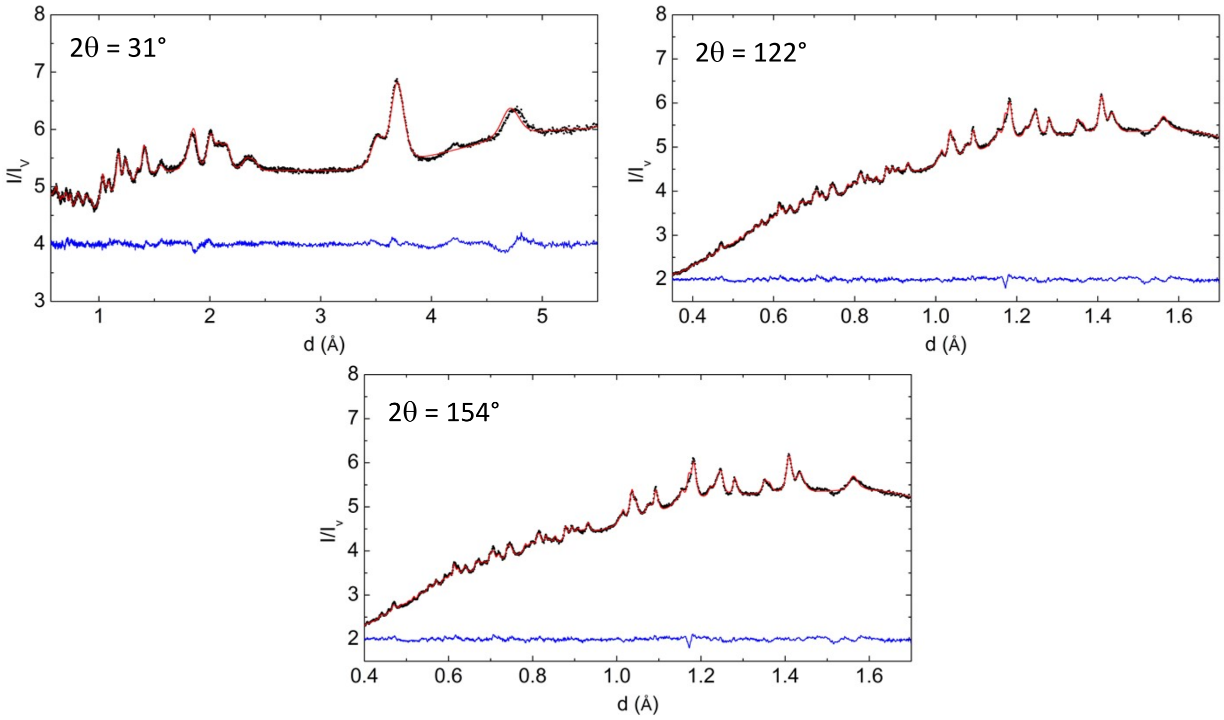

Figure S28. Rietveld refinement of structures of charged NMC811 (75%), lithiated graphite (at stage II and stage I), Cu and Al using *in situ* neutron diffraction data.

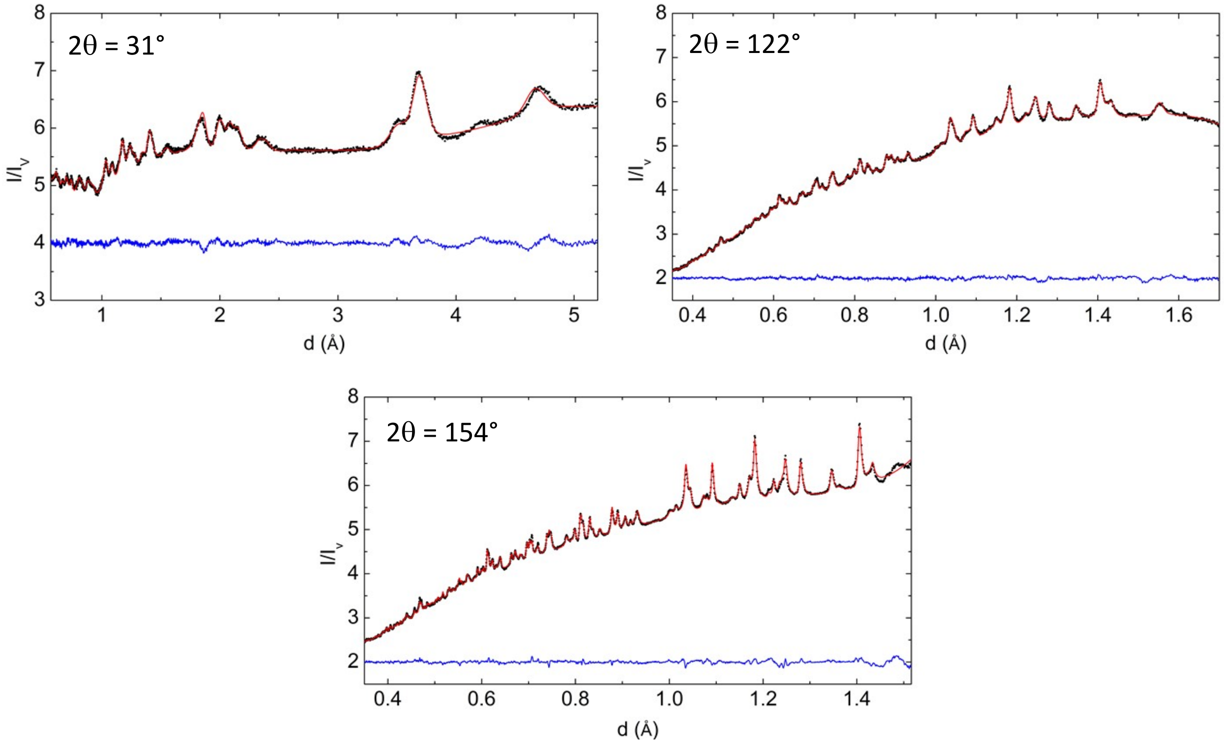

Figure S29. Rietveld refinement of structures of charged NCA (75%), lithiated graphite (at stage II and stage I), Cu and Al using *in situ* neutron diffraction data.

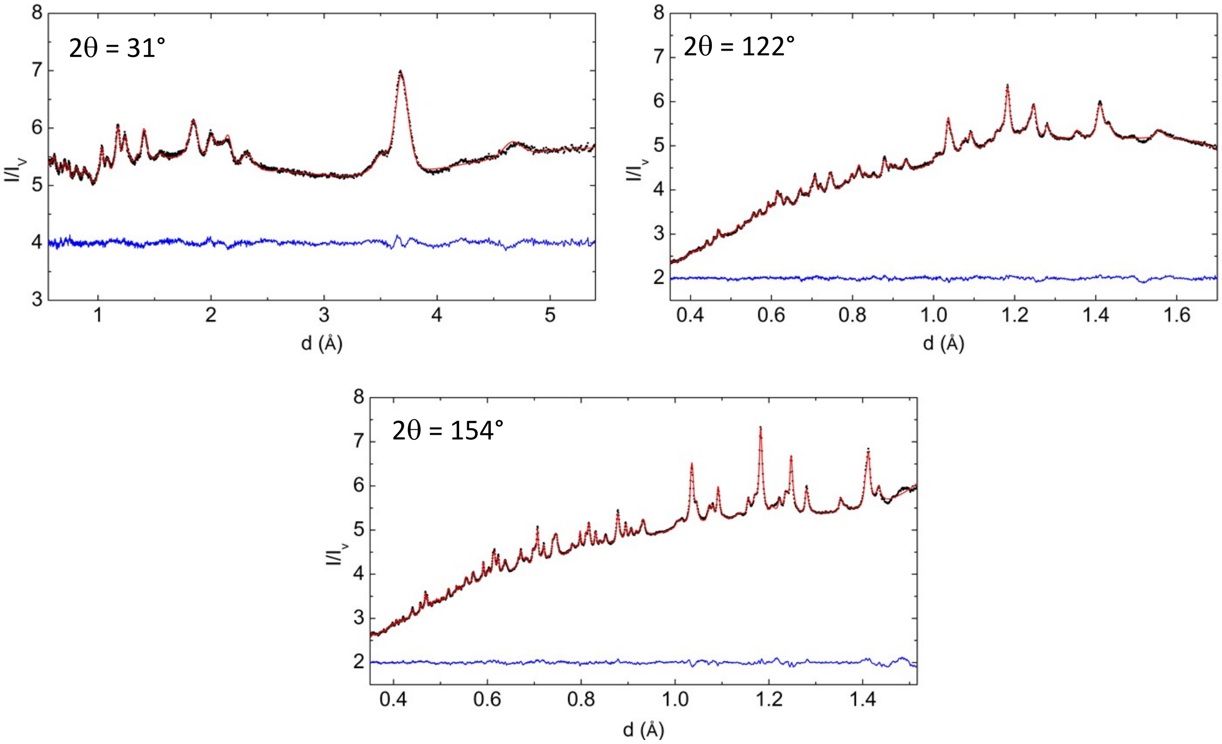

Figure S30. Rietveld refinement of structures of charged NMC532 (4.6V), lithiated graphite (stage I + limited residual stage II), Cu and Al using *in situ* neutron diffraction data.

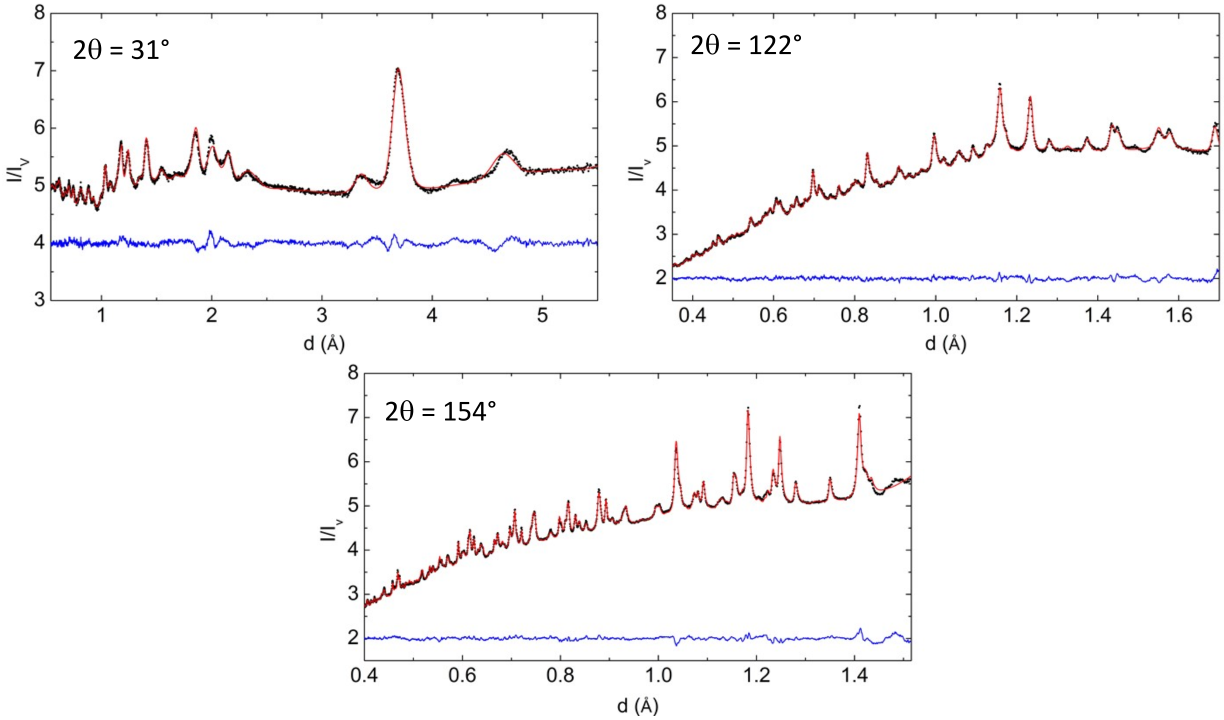

Figure S31. Rietveld refinement of structures of charged NMC622 (4.6 V), lithiated graphite (stage I and limited stage II), Cu and Al using *in situ* neutron diffraction data.

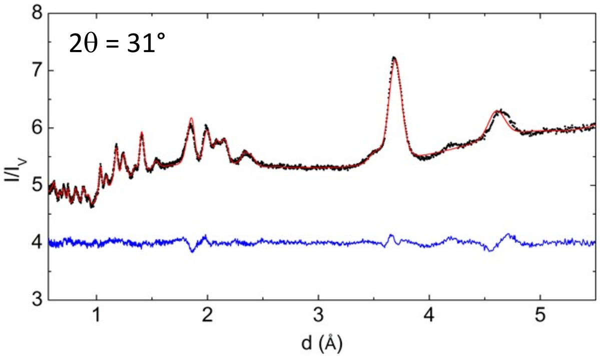

2θ = 122°

2θ = 154°

Figure S32. Rietveld refinement of structures of charged NMC811 (4.6 V), lithiated graphite (stage I), Cu and Al using *in situ* neutron diffraction data.

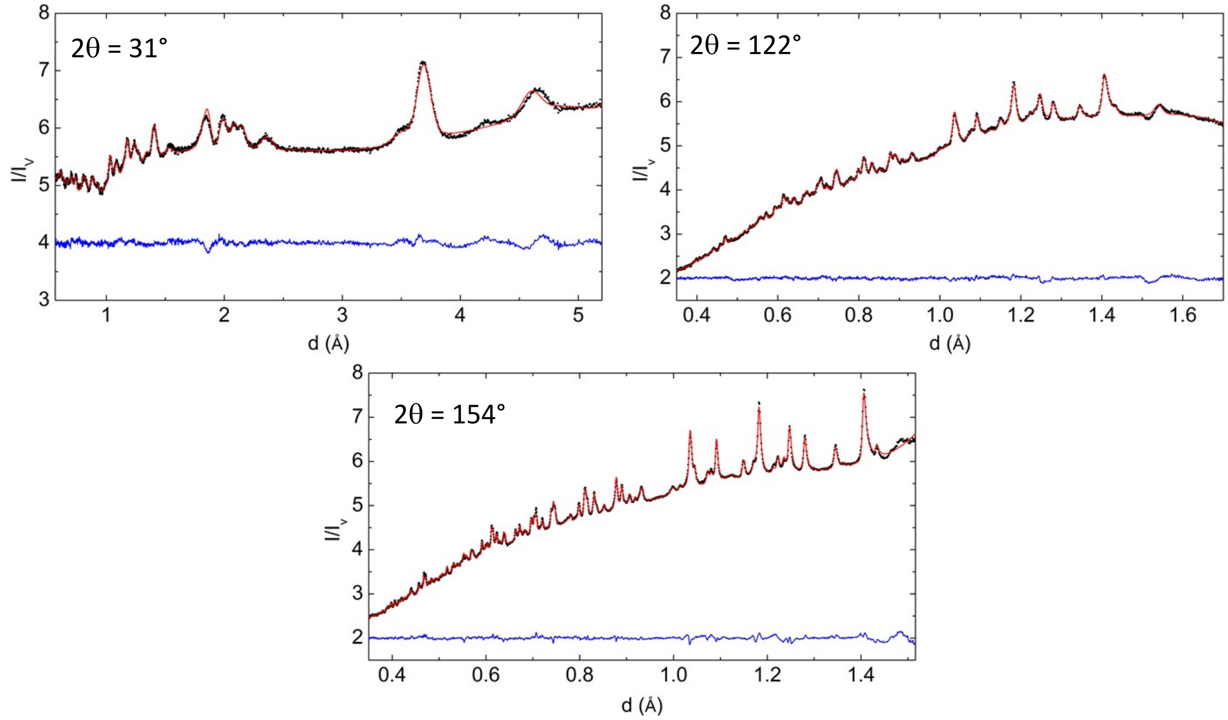

Figure S33. Rietveld refinement of structures of charged NCA (4.6 V), lithiated graphite (stage I), Cu and Al using *in situ* neutron diffraction data.

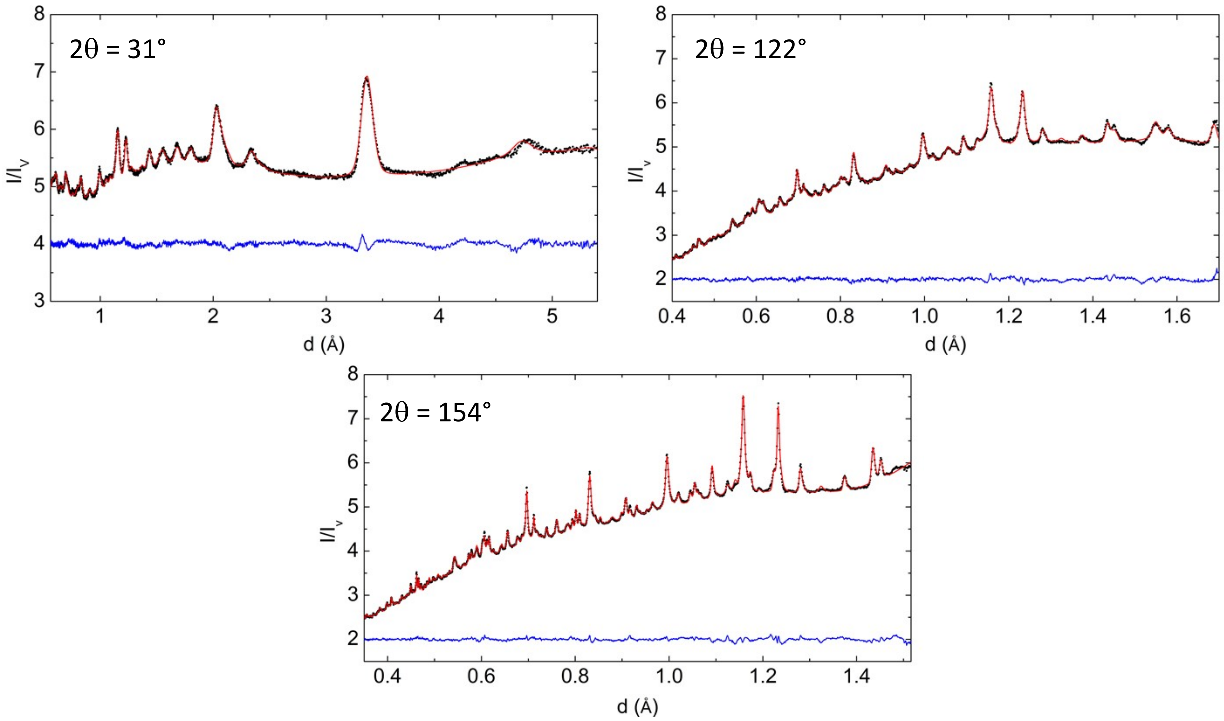

Figure S34. Rietveld refinement of structures of fully discharged NMC532 (2.8 V), graphite, Cu and Al using *in situ* neutron diffraction data.

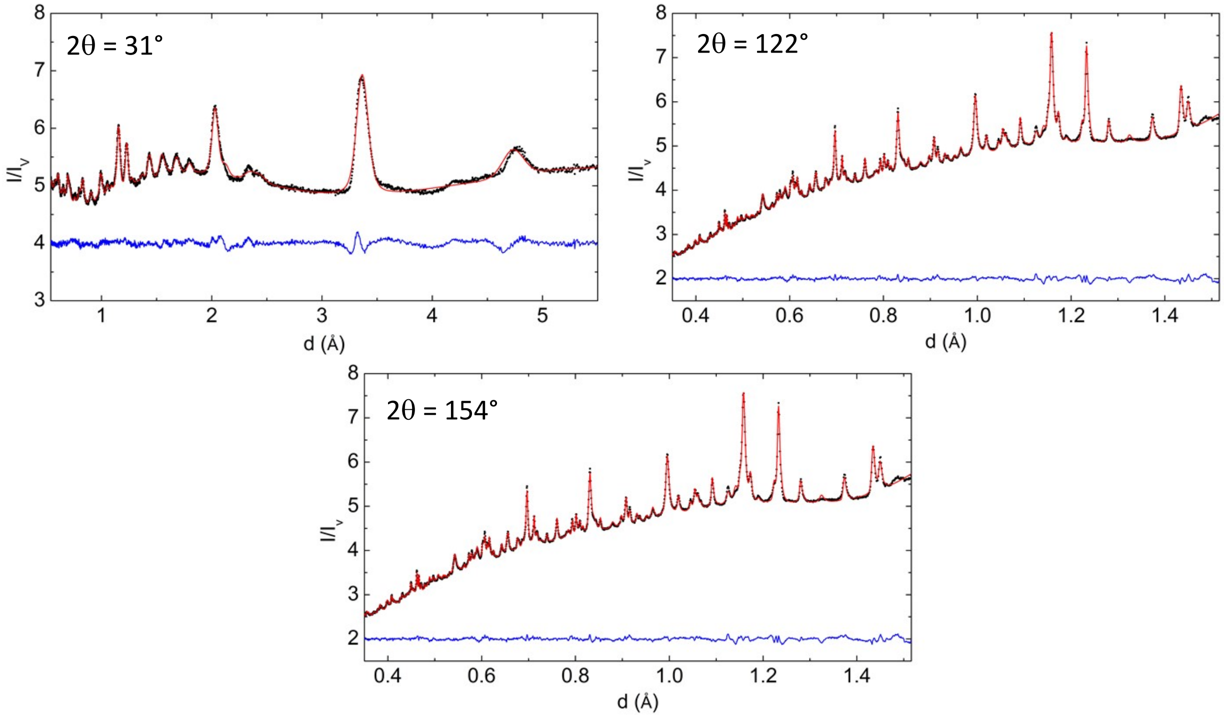

Figure S35. Rietveld refinement of structures of fully discharged NMC622 (2.8 V), graphite, Cu and Al using *in situ* neutron diffraction data.

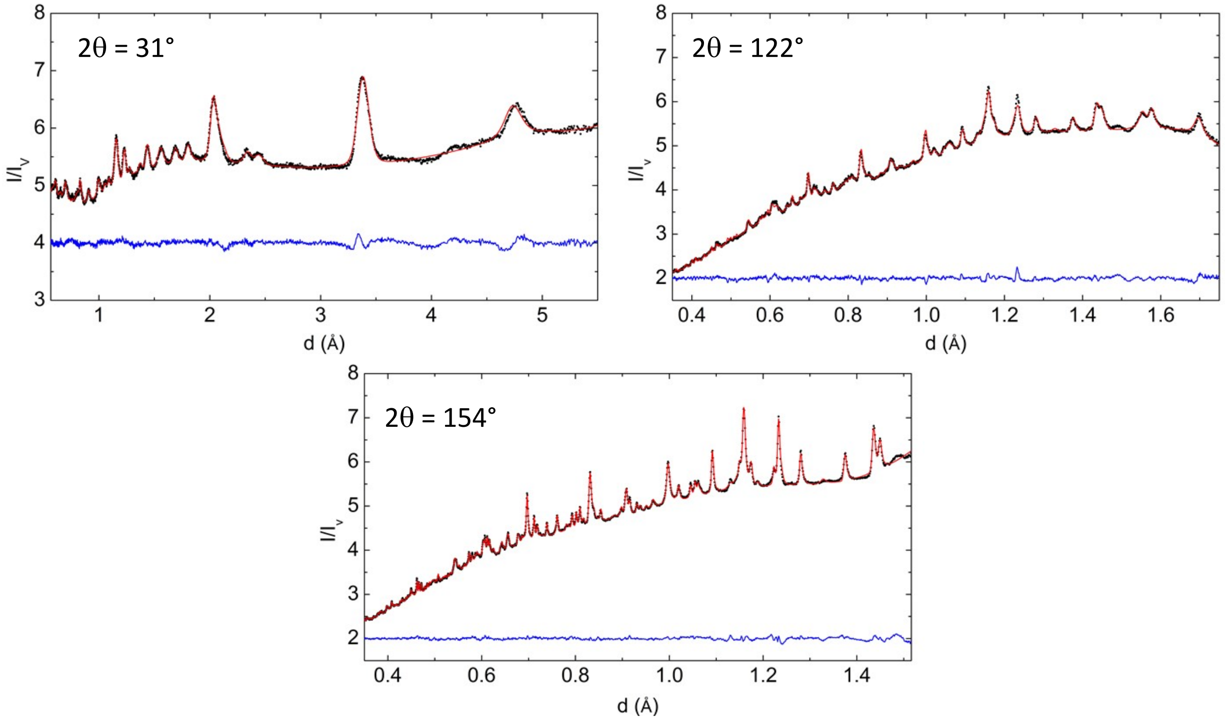

Figure S36. Rietveld refinement of structures of fully discharged NMC811 (2.8 V), graphite, Cu and Al using *in situ* neutron diffraction data.

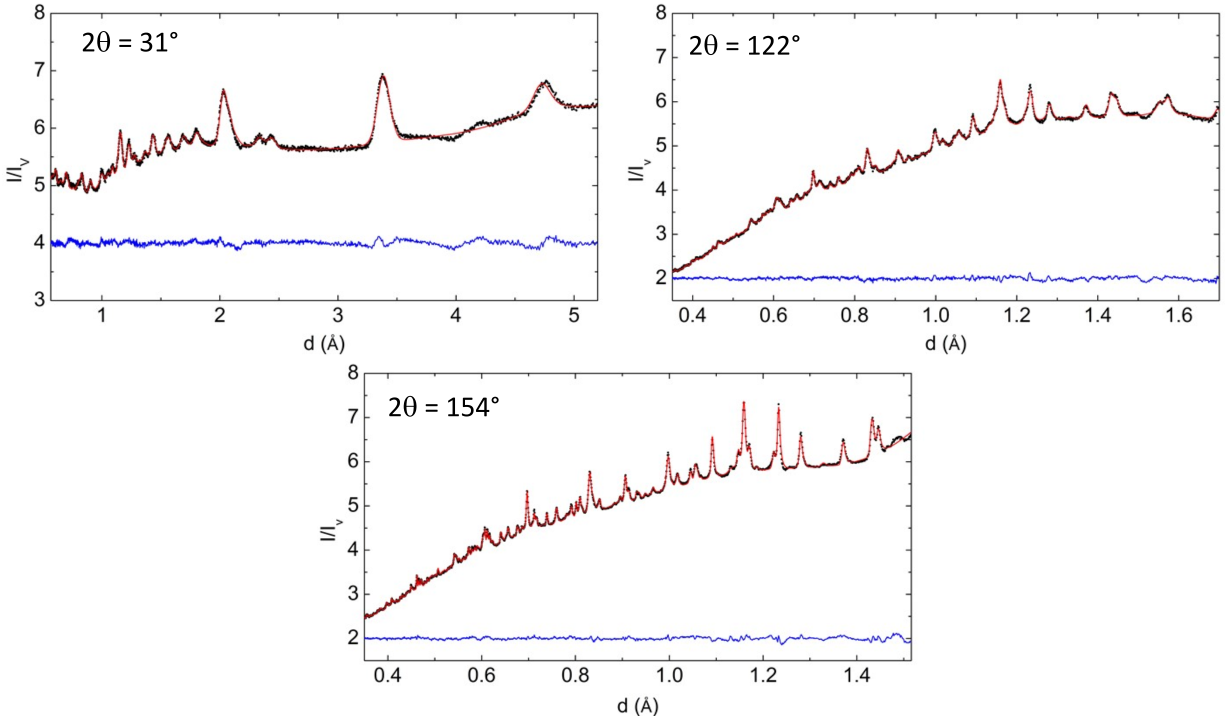

Figure S37. Rietveld refinement of structures of fully discharged NCA (2.8 V), graphite, Cu and Al using *in situ* neutron diffraction data.

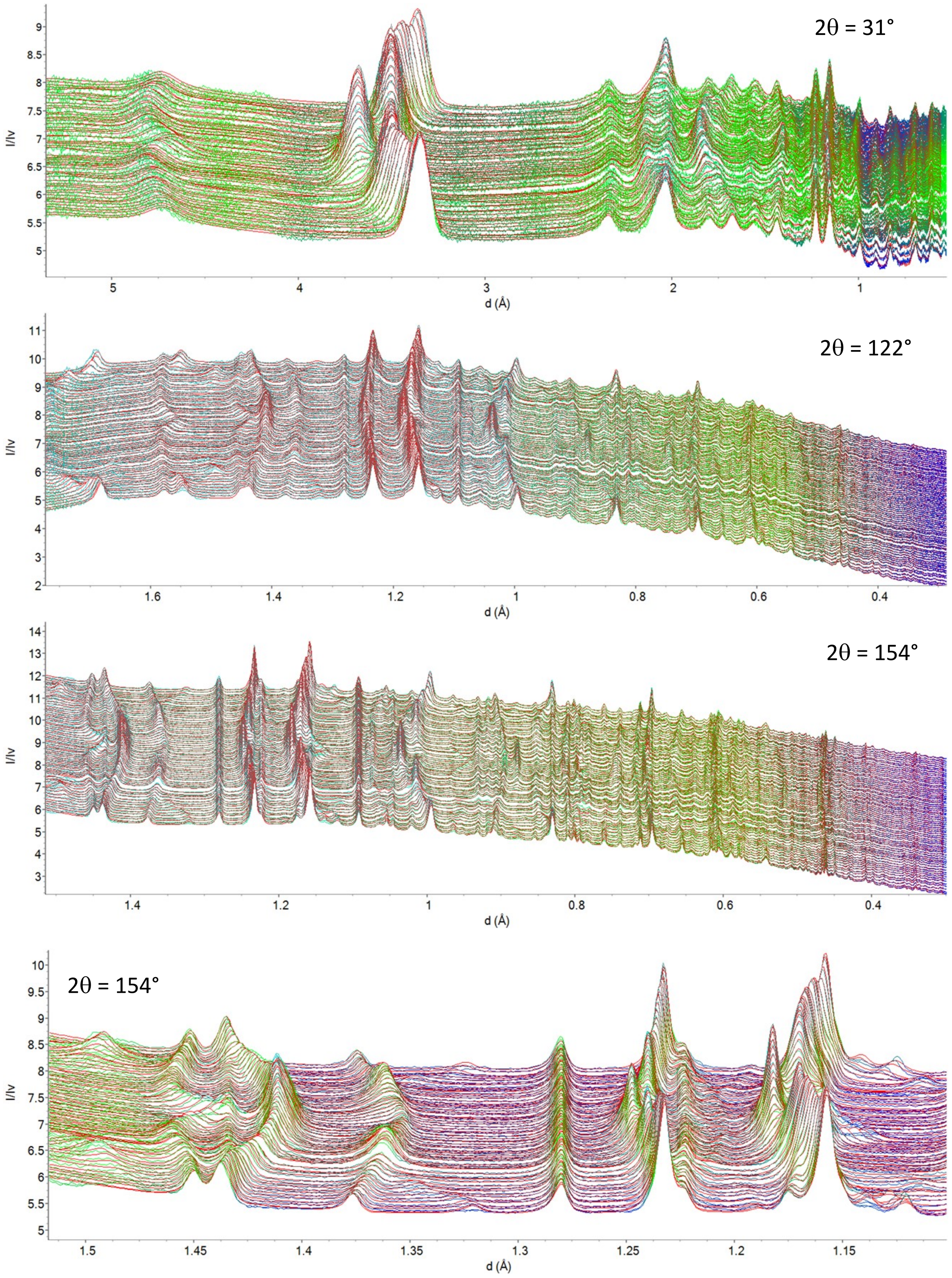

Figure S38. Parametric Rietveld refinements of structures of Li_{1-x}NMC532, (lithiated) graphite, Cu and Al during the initial cycle using three banks of neutron diffraction data from NOMAD (center 2θ = 31°, 122° and 154°). The last figure shows the enlarged regions of the high-resolution frame.

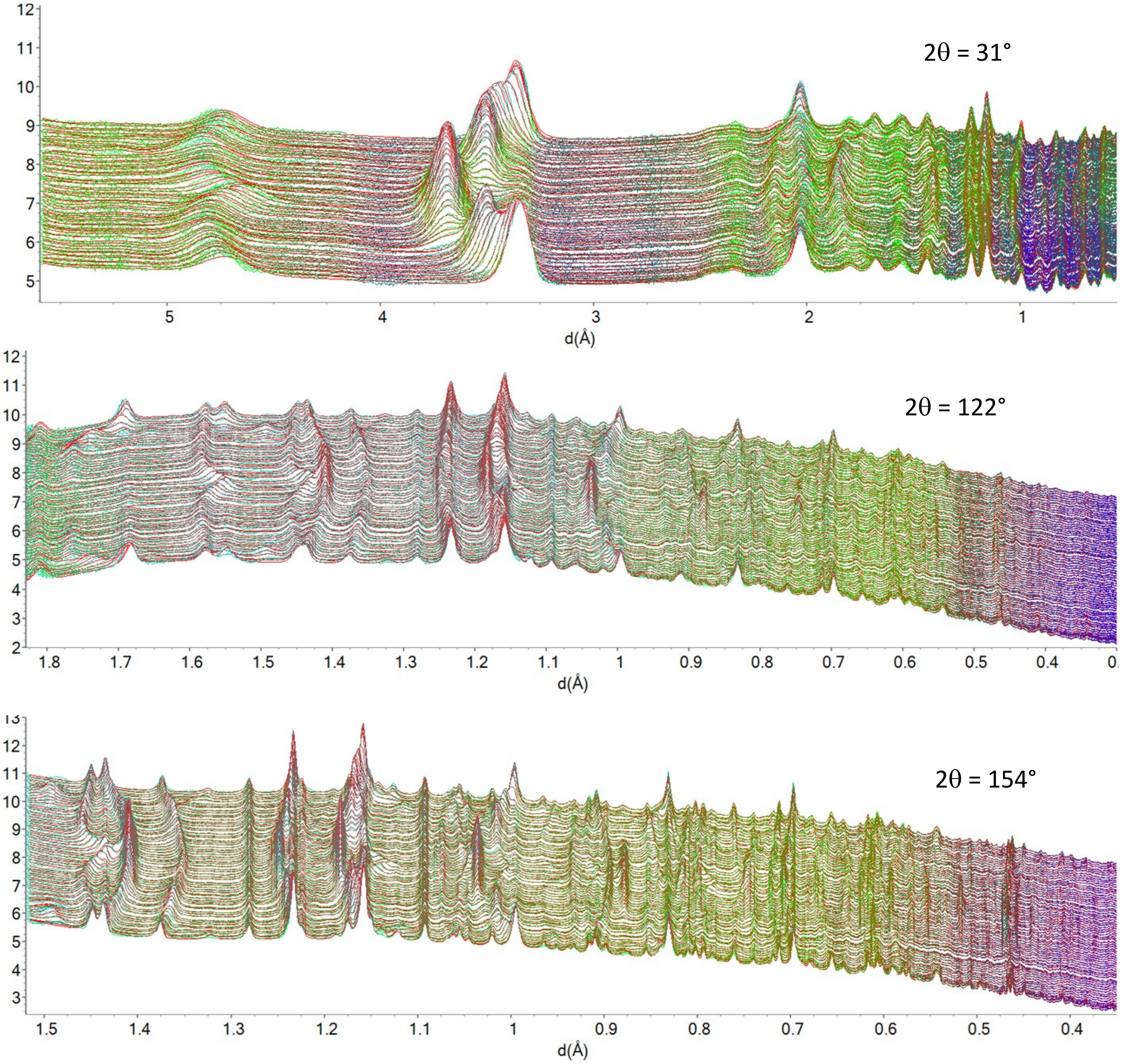

Figure S39. Parametric Rietveld refinements of structure of Li_{1-x}NMC622, (lithiated) graphite, Cu and Al during the initial cycle using three banks of neutron diffraction data from NOMAD (center 2θ = 31°, 122° and 154°).

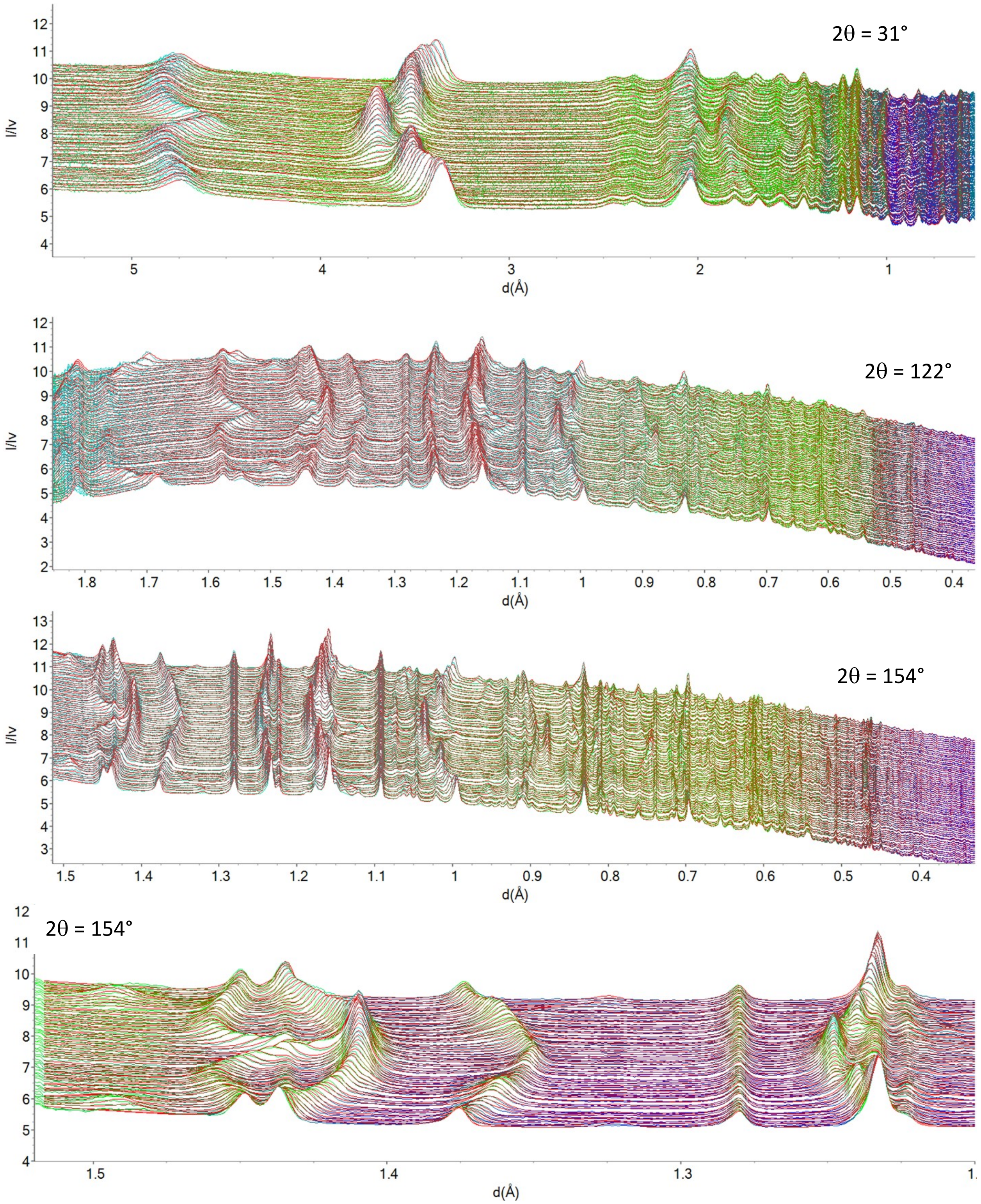

Figure S40. Parametric Rietveld refinements of structure of Li$_{1-x}$NMC811, (lithiated) graphite, Cu and Al during the first cycle using three banks of neutron diffraction data from NOMAD (center 2θ = 31°, 122° and 154°). The last figure shows the enlarged regions of the high-resolution frame.

2θ = 31°

2θ = 122°

2θ = 154°

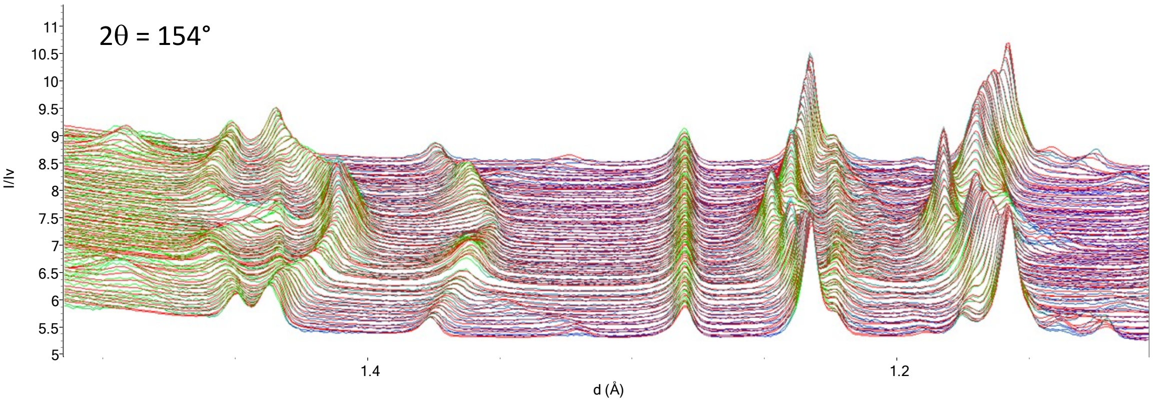

Figure S41. Parametric Rietveld refinements of structure of $Li_{1-x}NCA$ d, (lithiated) graphite, Cu and Al during the initial cycle using three banks of neutron diffraction data from NOMAD (center 2θ = 31°, 122° and 154°). The last figure shows the enlarged regions of the high-resolution frame.

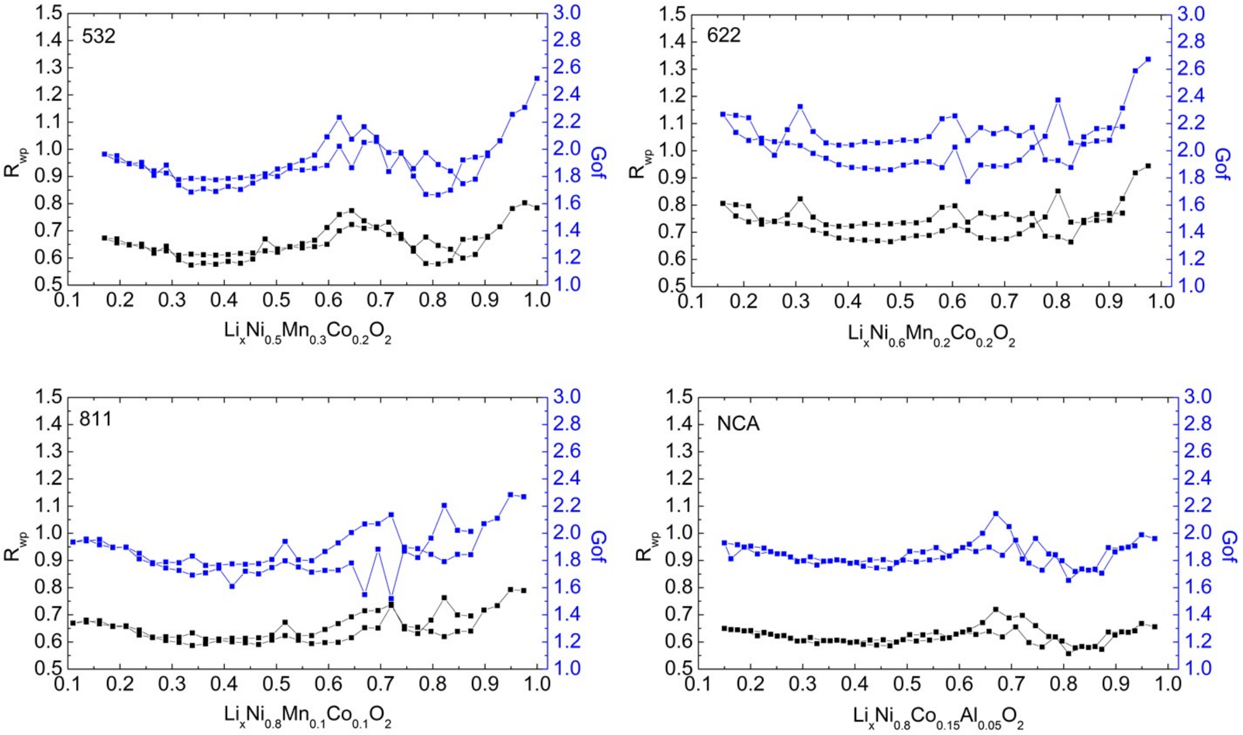

Figure S42. R_{wp} and goodness of fit (GOF) of Rietveld refinements of NMC532, NMC622, NMC811 and NCA (graphite, Cu and Al) during the initial charge and discharge.

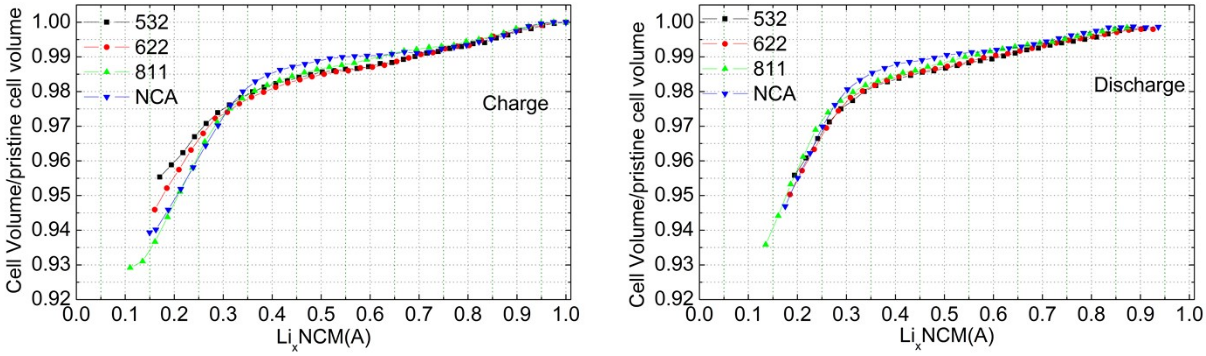

Figure S43. Normalized cell volume evolution during the initial charge (a) and discharge (b) of NMC532, NMC622, NMC811 and NCA. Cell volumes decrease almost linearly at $x < 0.3$, and the decreasing rate increase as a function of Ni concentration (e.g., NCA ~ NMC811 > NMC622 > NMC532).

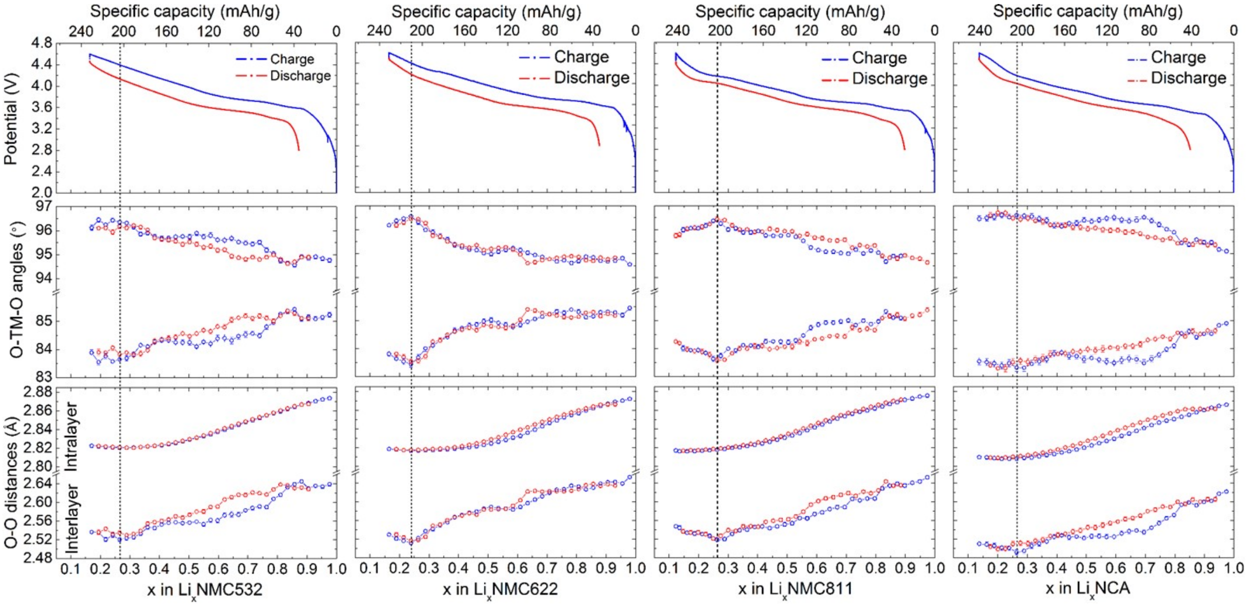

Figure S44. Evolution of O-O distances within TMO_2 slab, O-TM-O bond angles of NMC532, NMC622, NMC811 and NCA as a function of the state of charge and discharge. The dotted line highlights stage III to stage IV transitions.

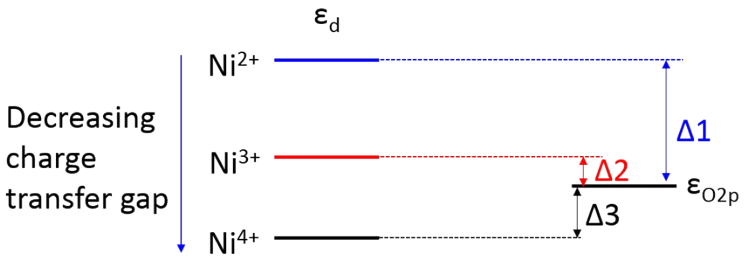

Figure S45. Schematic energy levels of oxygen 2p orbitals relative to the TM 3d orbitals.

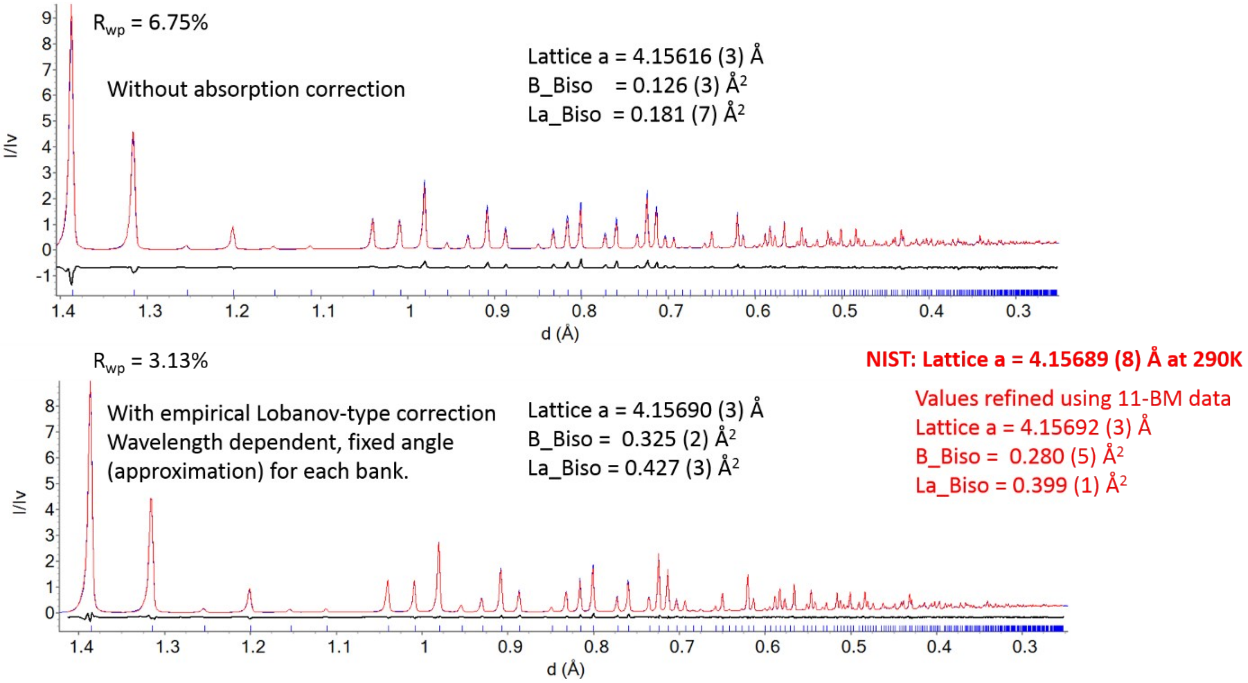

Figure S46. Structure refinements of La^{11}B$_{5.94}$^{10}B$_{0.06}$ with (bottom) and without (top) the empirical Lobanov-type absorption correction (high resolution frame with center 2θ = 154°).

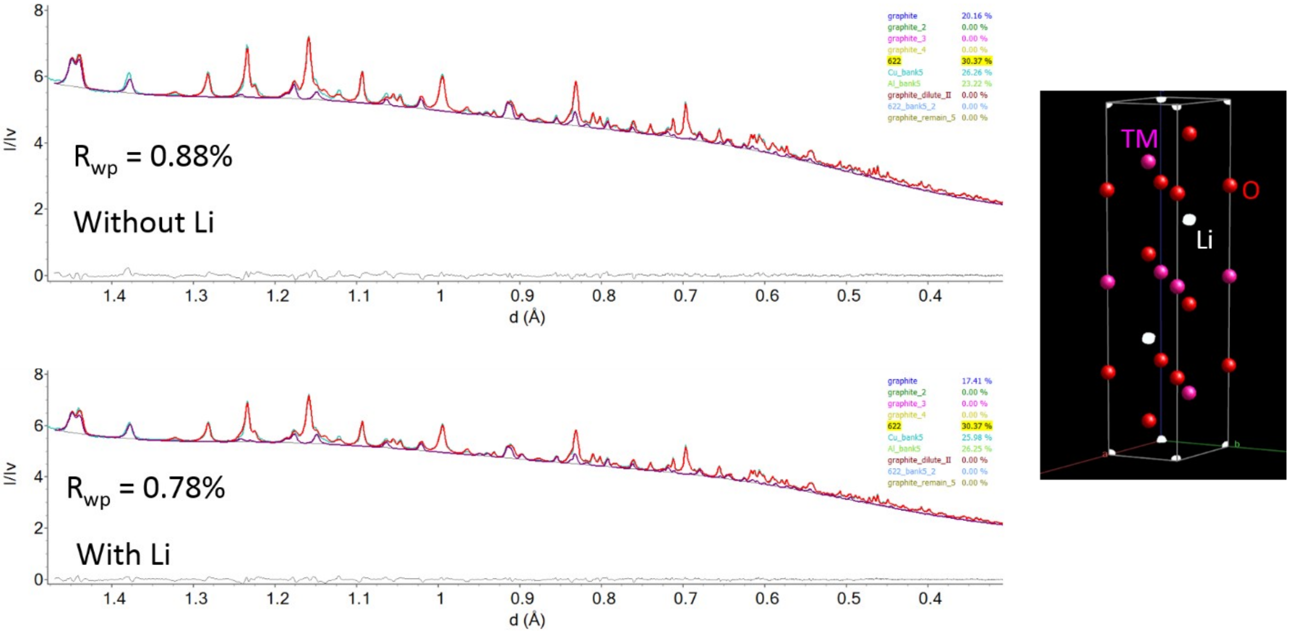

Figure S47. Left, structure refinements of NMC811 with (bottom) and without (top) Li using *in situ* neutron diffraction data collected before charging. Right, Fourier difference map showing the residual nuclear scattering lengths of Li from the structure refinement without Li.

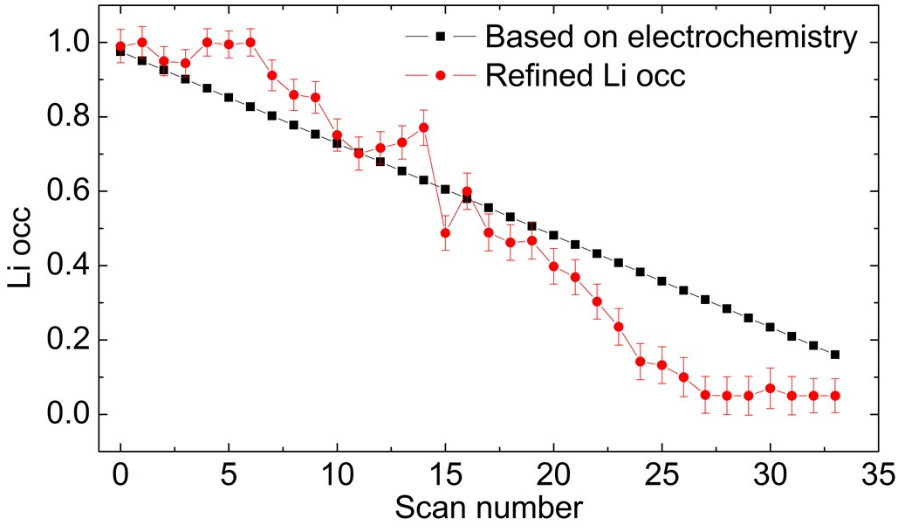

Figure S48. The refined lithium occupancies (red) plotted as a function of the degree of delithiation in $Li_{1-x}Ni_{0.6}Mn_{0.2}Co_{0.2}O_2$ (4.6 V versus graphite). The overall trend matches reasonably well with the values obtained from electrochemistry data (black) at a relatively low degrees of delithiation but the deviation becomes significant at high degrees of delithiation. This is very likely due to the change of lithium mobility during delithiation.

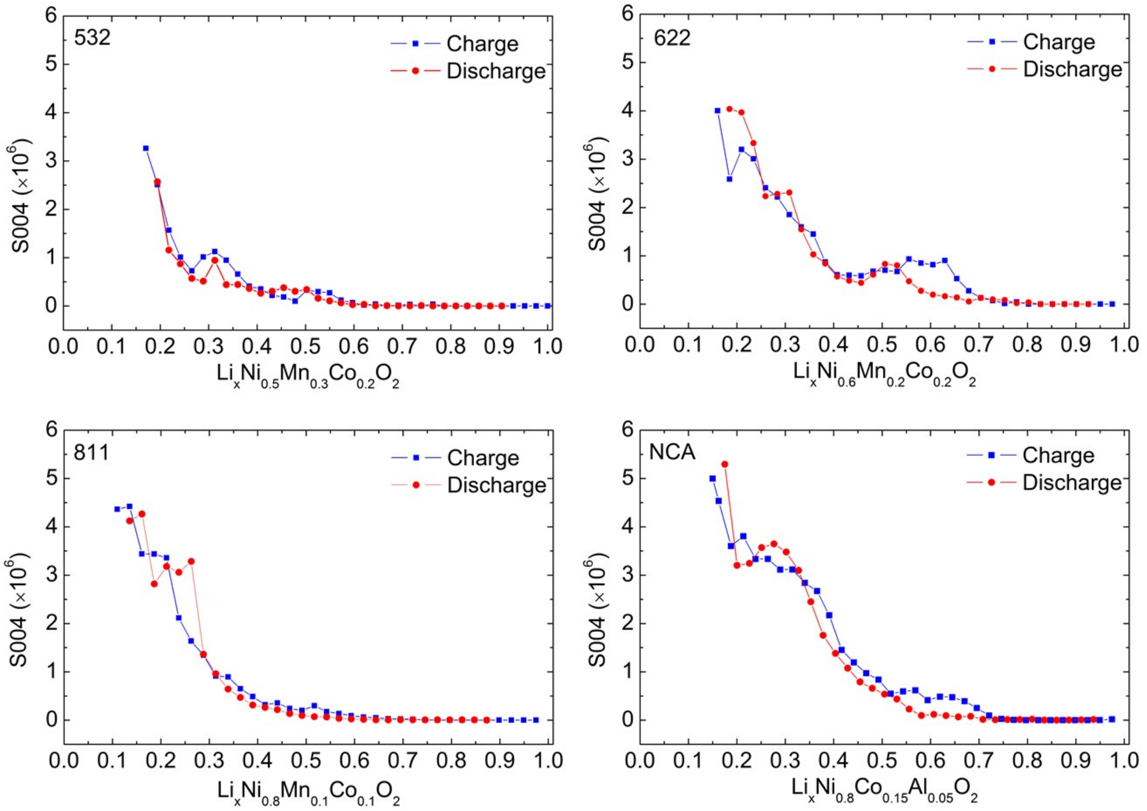

Figure S49. The refined S004 of Stephen's anisotropic strain broadening model for NMC532, 622, 811 and NCA during initial charge and discharge.

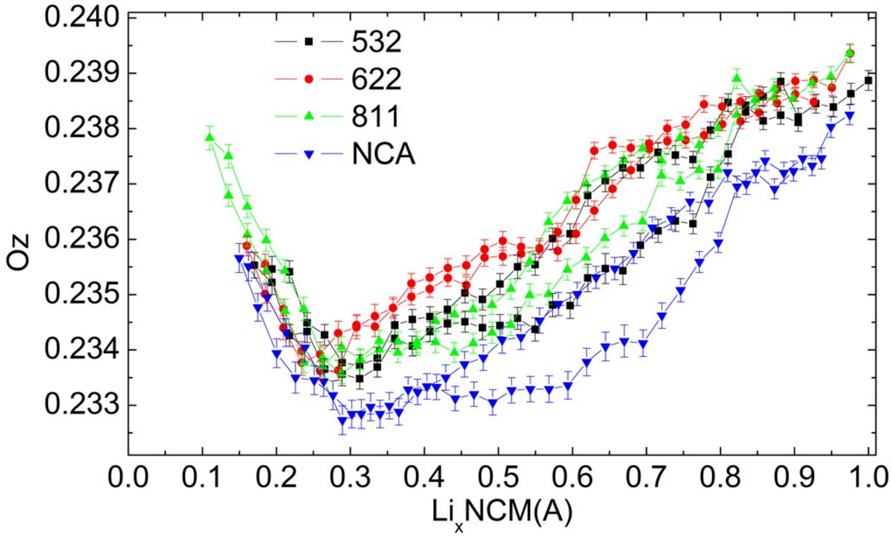

Figure S50. Refined O_z of NMC532, NMC622, NMC811 and NCA during the initial charge and discharge.

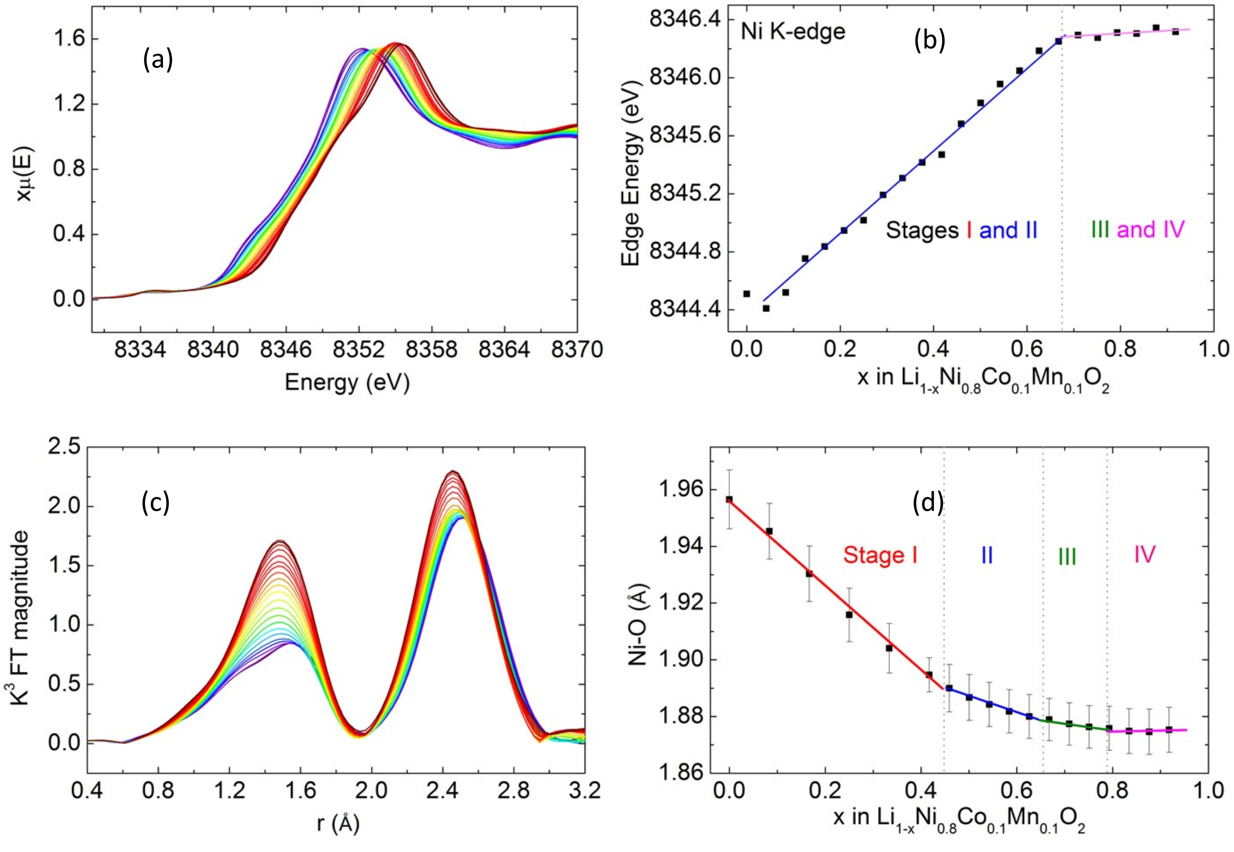

Figure S51. (a) Ni K-edge XANES during the initial charge of $LiNi_{0.8}Mn_{0.1}Co_{0.2}O_2$ (versus Li^+/Li) to 4.8 V. (b) the change of Ni K-edge energy as a function of delithiation. (c) The evolution of Ni-O and Ni-Me distances obtained from Ni K-edge EXAFS. (d) Refined average Ni-O bond lengths evolution in NMC811.

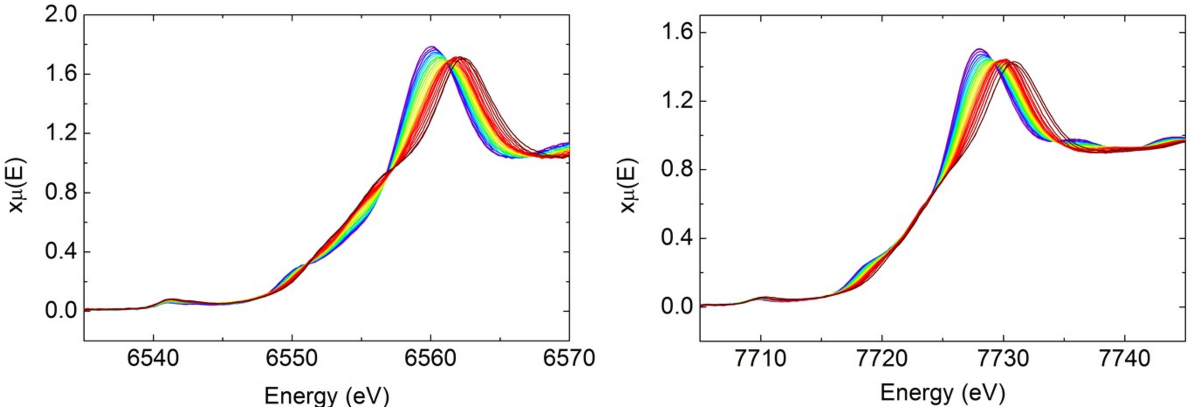

Figure S52. (a) Mn and (b) Co K-edge XANES during the initial charge of $LiNi_{0.8}Mn_{0.1}Co_{0.2}O_2$ (versus Li^+/Li) to 4.8 V.

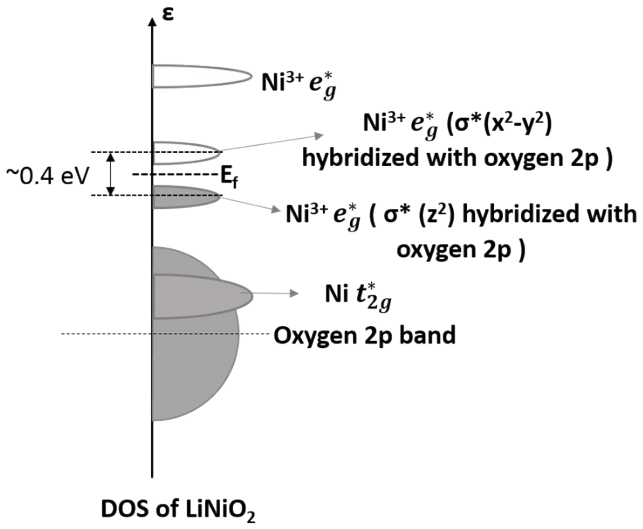

Figure S53. Schematic density of states of $LiNiO_2$.

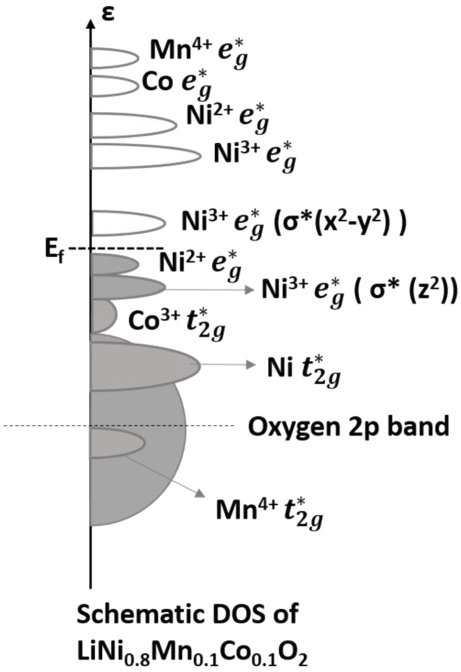

Figure S54. Schematic density of states of NMC811 with Mn^{4+} contribution.

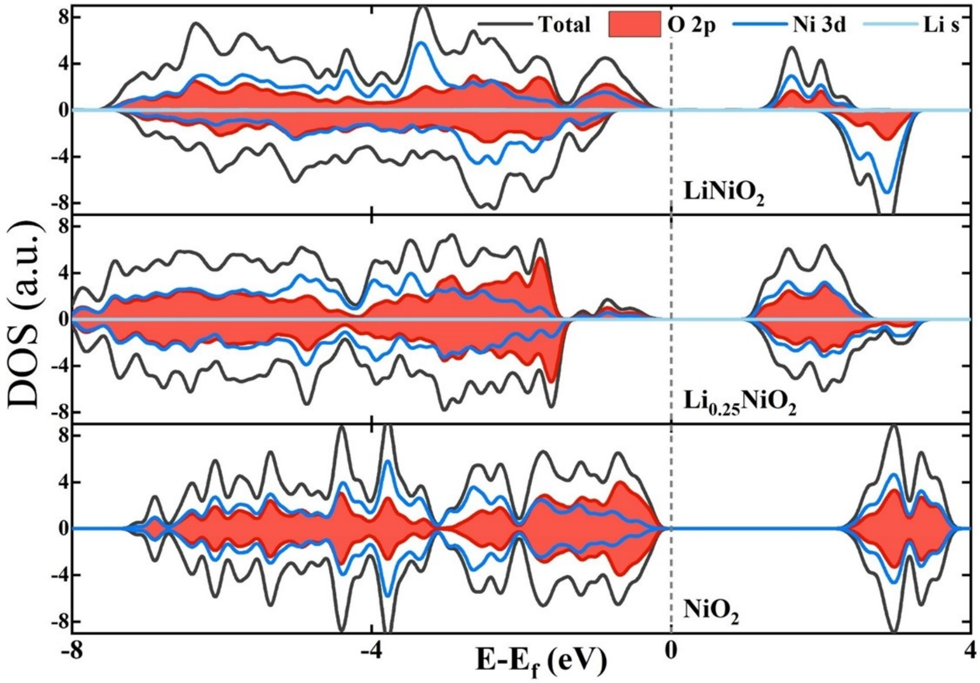

Figure S55. Calculated density of states of Li_xNiO_2 at the SOC of 0% (x=1), 75% (x=0.25) and 100% (x=0). It can be seen that the front of the valence band is dominated by oxygen 2p character in the 75% and fully charged Li_xNiO_2. It is also worth noting that there is an intermediate state (though not completely separated from the major valence band) in the $Li_{0.25}NiO_2$, suggesting that the formation of spin singlet states is the most likely electronic structure in stages III and IV.

Table S1. Key structure information of pristine NMCs and NCA refined using powder neutron diffraction data.

	a (Å)	c (Å)	TM-O (Å)	Li-O (Å)	TMO_2 slab thickness (Å)	LiO_2 slab thickness (Å)	Ni_{Li} anti-site
NMC532	2.87003(4)	14.2452(2)	1.9693(2)	2.1124(2)	2.1281(7)	2.6204(7)	0.042(1)
NMC622	2.86917(3)	14.2190(2)	1.9663(2)	2.1123(2)	2.1184(6)	2.6212(6)	0.023(1)
NMC811	2.87213(2)	14.2082(1)	1.9665(2)	2.1139(2)	2.1141(6)	2.6220(6)	0.016(1)
NCA	2.86272(2)	14.1830(1)	1.9574(2)	2.1121(2)	2.0974(6)	2.6301(6)	0.008(1)

Table S2. Refined structure of NMC532 using multiple bank NOMAD data (R_{wp} = 2.89%, gof = 4.05).

S.G. *R*-3m a = 2.87003(4) Å c = 14.2452(2) Å

Atom	Wyck.	*x*	*y*	*z*	Occ.	B_{eq} (Å^2)
Li1	3	0	0	0	0.958(1)	1.29(3)
Ni2	3	0	0	0	0.042(1)	1.29(3)
Co1	3	0	0	0.5	0.2	0.30(1)
Ni1	3	0	0	0.5	0.458(1)	0.30(1)
Mn1	3	0	0	0.5	0.3	0.30(1)
Li2	3	0	0	0.5	0.042(1)	0.30(1)
O1	6	0	0	0.24136(2)	1	0.72(1)

Table S3. Refined structure of NMC622 using multiple bank NOMAD data (R_{wp} = 2.38%, gof = 3.80).

S.G. *R*-3m a = 2.86917(3) Å c = 14.2190(2) Å

Atom	Wyck.	*x*	*y*	*z*	Occ.	B_{eq} (Å^2)
Li1	3	0	0	0	0.977(1)	1.37(2)
Ni2	3	0	0	0	0.023(1)	1.37(2)
Co1	3	0	0	0.5	0.2	0.26(1)
Ni1	3	0	0	0.5	0.577(1)	0.26(1)
Mn1	3	0	0	0.5	0.2	0.26(1)
Li2	3	0	0	0.5	0.023(1)	0.26(1)
O1	6	0	0	0.24116(2)	1	0.80(1)

Table S4. Refined structure of NMC811 using multiple bank NOMAD data (R_{wp} = 2.41%, gof = 4.19).

S.G. *R*-3m a = 2.87213(2) Å c = 14.2082(1) Å

Atom	Wyck.	*x*	*y*	*z*	Occ.	B_{eq} (Å^2)
Li1	3	0	0	0	0.984(1)	1.16(2)
Ni2	3	0	0	0	0.016(1)	1.16(2)
Co1	3	0	0	0.5	0.1	0.30(1)
Ni1	3	0	0	0.5	0.784(1)	0.30(1)
Mn1	3	0	0	0.5	0.1	0.30(1)

Li2	3	0	0	0.5	0.016(1)	0.30(1)
O1	6	0	0	0.24106(2)	1	0.78(1)

Table S5. Refined structure of NCA using multiple bank NOMAD data (R_{wp} = 2.44%, gof = 3.73).

S.G. *R*-3m a = 2.86272(2) Å c = 14.1830(1) Å

Atom	Wyck.	*x*	*y*	*z*	Occ.	B_{eq} (Å^2)
Li1	3	0	0	0	0.992(1)	1.13(2)
Ni2	3	0	0	0	0.008(1)	1.13(2)
Co1	3	0	0	0.5	0.15	0.29(1)
Ni1	3	0	0	0.5	0.792(1)	0.29(1)
Mn1	3	0	0	0.5	0.05	0.29(1)
Li2	3	0	0	0.5	0.008(1)	0.29(1)
O1	6	0	0	0.24060(2)	1	0.75(1)

Table S6. Key structure information of pristine NMCs and NCA refined using *in situ* neutron diffraction data collected before charging.

	a (Å)	c (Å)	TM-O (Å)	Li-O (Å)	TMO_2 slab thickness (Å)	LiO_2 slab thickness (Å)	Ni_{Li} anti-site*
NMC532	2.8724(2)	14.2658(2)	1.9504(12)	2.1390(20)	2.06415(4)	2.7018(50)	0.042
NMC622	2.8719(2)	14.2408(7)	1.9496(16)	2.1367(19)	2.0511(60)	2.6956(61)	0.023
NMC811	2.8755(1)	14.2251(8)	1.9559(13)	2.1314(15)	2.0683(48)	2.6734(48)	0.016
NCA	2.8657(1)	14.2024(9)	1.9419(14)	2.1357(16)	2.0333(52)	2.7009(52)	0.008

* Fixed to the values refined using *ex situ* neutron diffraction data

Table S7. Refined structure of pristine NMC532 using *in situ* neutron diffraction data collected before charging (R_{wp} = 0.78%, gof=2.52).

S.G. *R*-3m a = 2.8724(2) Å c = 14.2658(2) Å

Atom	Wyck.	*x*	*y*	*z*	Occ.	B_{eq} (Å^2)
Li1	3	0	0	0	0.958	1.97(23)
Ni2	3	0	0	0	0.042	1.97(23)
Co1	3	0	0	0.5	0.2	0.46(10)
Ni1	3	0	0	0.5	0.458	0.46(10)
Mn1	3	0	0	0.5	0.3	0.46(10)

Li2	3	0	0	0.5	0.042	0.46(10)
O1	6	0	0	0.2389(12)	1	0.74(6)

Table S8. Refined structure of pristine NMC622 using *in situ* neutron diffraction data collected before charging (R_{wp} = 0.94%, gof=2.67).

S.G. R-3m a = 2.8719(2) Å c = 14.2408(7) Å						
Atom	Wyck.	x	y	z	Occ.	B_{eq} (Å^2)
Li1	3	0	0	0	0.977	1.69(25)
Ni2	3	0	0	0	0.023	1.69(25)
Co1	3	0	0	0.5	0.2	0.32(7)
Ni1	3	0	0	0.5	0.577	0.32(7)
Mn1	3	0	0	0.5	0.2	0.32(7)
Li2	3	0	0	0.5	0.023	0.32(7)
O1	6	0	0	0.2387(22)	1	0.70(6)

Table S9. Refined structure of pristine NMC811 using *in situ* neutron diffraction data collected before charging (R_{wp} = 0.78%, gof = 2.27).

S.G. R-3m a = 2.8755(1) Å c = 14.2251(8) Å						
Atom	Wyck.	x	y	z	Occ.	B_{eq} (Å^2)
Li1	3	0	0	0	0.958	1.53(20)
Ni2	3	0	0	0	0.016	1.53(20)
Co1	3	0	0	0.5	0.1	0.40(6)
Ni1	3	0	0	0.5	0.784	0.40(6)
Mn1	3	0	0	0.5	0.1	0.40(6)
Li2	3	0	0	0.5	0.016	0.40(6)
O1	6	0	0	0.2394(17)	1	0.67(6)

Table S10. Refined structure of pristine NCA using *in situ* neutron diffraction data collected before charging (R_{wp} = 0.66%, gof = 1.96).

S.G. R-3m a = 2.8657(1) Å c = 14.2024(9) Å						
Atom	Wyck.	x	y	z	Occ.	B_{eq} (Å^2)
Li1	3	0	0	0	0.992(1)	1.67(24)
Ni2	3	0	0	0	0.008(1)	1.67(24)
Co1	3	0	0	0.5	0.15	0.29(5)
Ni1	3	0	0	0.5	0.792(1)	0.29(5)
Mn1	3	0	0	0.5	0.05	0.29(5)
Li2	3	0	0	0.5	0.008(1)	0.29(5)
O1	6	0	0	0.2383(18)	1	0.59(6)

Table S11. Key structure information of 4.6 V charged NMCs and NCA refined using *in situ* neutron diffraction data collected before charging.

	a (Å)	c (Å)	TM-O (Å)	Li-O (Å)	TMO_2 slab thickness (Å)	LiO_2 slab thickness (Å)
NMC532	2.8227(2)	14.1179(20)	1.8976(17)	2.1360(21)	1.9443(65)	2.7617(65)
NMC622	2.8183(3)	13.9892(20)	1.8922(19)	2.1244(24)	1.9315(73)	2.7316(73)
NMC811	2.8167(1)	13.7755(25)	1.8988(15)	2.0918(18)	1.9605(58)	2.1141(58)
NCA	2.8096(1)	13.8784(33)	1.8836(18)	2.1140(23)	1.9150(73)	2.7111(73)

Table S12. Refined structure of 4.6V charged NMC532 using *in situ* neutron diffraction data collected before charging (R_{wp} = 0.67%, gof = 1.96).

S.G. *R*-3m a = 2.8227(2) Å c = 14.1179(20) Å						
Atom	Wyck.	*x*	*y*	*z*	Occ.	B_{eq} ($Å^2$)
Li1	3	0	0	0	0.171	1.99(23)
Ni2	3	0	0	0	0.042	1.99(23)
Co1	3	0	0	0.5	0.2	0.33(10)
Ni1	3	0	0	0.5	0.458	0.33(10)
Mn1	3	0	0	0.5	0.3	0.33(10)
Li2	3	0	0	0.5	0	0.33(10)
O1	6	0	0	0.2355(2)	1	0.40(5)

Table S13. Refined structure of 4.6 V charged NMC622 using *in situ* neutron diffraction data collected before charging (R_{wp} = 0.81%, gof = 2.27).

S.G. *R*-3m a = 2.8183(3) Å c = 13.9892(20) Å						
Atom	Wyck.	*x*	*y*	*z*	Occ.	B_{eq} ($Å^2$)
Li1	3	0	0	0	0.160	2.00(81)
Ni2	3	0	0	0	0.023	2.00(81)
Co1	3	0	0	0.5	0.2	0.22(5)
Ni1	3	0	0	0.5	0.577	0.22(5)
Mn1	3	0	0	0.5	0.2	0.22(5)
Li2	3	0	0	0.5	0	0.22(5)
O1	6	0	0	0.2357(3)	1	0.41(4)

Table S14. Refined structure of 4.6 V charged NMC811 using *in situ* neutron diffraction data collected before charging (R_{wp} = 0.67%, gof = 1.94).

S.G. *R*-3m a = 2.8167(1) Å c = 13.7755(25) Å						
Atom	Wyck.	*x*	*y*	*z*	Occ.	B_{eq} ($Å^2$)
Li1	3	0	0	0	0.110	1.93(80)
Ni2	3	0	0	0	0.016	1.93(80)
Co1	3	0	0	0.5	0.1	0.25(6)

Ni1	3	0	0	0.5	0.784	0.25(6)
Mn1	3	0	0	0.5	0.1	0.25(6)
Li2	3	0	0	0.5	0	0.25(6)
O1	6	0	0	0.2394(17)	1	0.67(6)

Table S15. Refined structure of 4.6 V charged NCA using *in situ* neutron diffraction data collected before charging (R_{wp} = 0.65%, gof=1.93).

S.G. *R*-3m a = 2.8096(1) Å c = 13.8784(33) Å						
Atom	Wyck.	*x*	*y*	*z*	Occ.	B_{eq} (Å^2)
Li1	3	0	0	0	0.150	1.67(64)
Ni2	3	0	0	0	0.008	1.67(64)
Co1	3	0	0	0.5	0.15	0.20(5)
Ni1	3	0	0	0.5	0.792	0.20(5)
Mn1	3	0	0	0.5	0.05	0.20(5)
Li2	3	0	0	0.5	0	0.20(5)
O1	6	0	0	0.2357(3)	1	0.40(7)

Table S16. Key structural parameters of 4.6 V charged (*ex situ*) NMCs and NCA (versus graphite) refined using powder neutron diffraction data*.

	a (Å)	c (Å)	TM-O (Å)	Li-O (Å)	TM-O thickness (Å)	Li-O thickness(Å)	Occ Li
NMC532	2.81960(8)	14.1017(5)	1.9000(3)	2.1280(3)	1.9596(11)	2.7410(11)	0.211(6)
NMC622	2.81328(5)	14.1426(3)	1.8955(2)	2.1123(2)	1.9541(9)	2.7600(9)	0.204(5)
NMC811	2.81351(6)	13.8289(6)	1.8916(4)	2.1029(5)	1.9387(16)	2.6708(16)	0.118(8)
NCA	2.80792(5)	14.1524(4)	1.8907(3)	2.1328(4)	1.9458(11)	2.7717(11)	0.183(7)

* note that the degree of delithiation may differ from the *in situ* cell even charged to the same cut-off voltage.

Table S17. Structure of 4.6 V charged NMC532 refined using multiple bank NOMAD data (R_{wp} = 1.92%, gof = 6.72)

S.G. *R*-3m a =2.81960(8) Å c = 14.1017(5) Å						
Atom	Wyck.	*x*	*y*	*z*	Occ.	B_{eq} (Å^2)
Li1	3	0	0	0	0.211(6)	1.29(24)
Ni2	3	0	0	0	0.040	1.29(24)
Co1	3	0	0	0.5	0.2	0.23(1)
Ni1	3	0	0	0.5	0.458	0.23(1)

Mn1	3	0	0	0.5	0.3	0.23(1)
Li2	3	0	0	0.5	0	0.23(1)
O1	6	0	0	0.23602(3)	1	0.42(1)

Table S18. Structure of 4.6 V charged NMC622 refined using multiple bank NOMAD data (R_{wp} = 2.23%, gof = 6.31)

S.G. *R*-3m a = 2.81328(5) Å c = 14.1426(3) Å						
Atom	Wyck.	*x*	*y*	*z*	Occ.	B_{eq} (Å^2)
Li1	3	0	0	0	0.204(5)	1.37(22)
Ni2	3	0	0	0	0.028(3)	1.37(22)
Co1	3	0	0	0.5	0.2	0.18(1)
Ni1	3	0	0	0.5	0.572(3)	0.18(1)
Mn1	3	0	0	0.5	0.2	0.18(1)
Li2	3	0	0	0.5	0	0.18(1)
O1	6	0	0	0.23574(3)	1	0.50(1)

Table S19. Structure of 4.6 V charged NMC811 refined using multiple bank NOMAD data (R_{wp} = 2.79%, gof = 9.34)

S.G. *R*-3m a = 2.81351(6) Å c = 13.8289(6) Å						
Atom	Wyck.	*x*	*y*	*z*	Occ.	B_{eq} (Å^2)
Li1	3	0	0	0	0.118(8)	1.16(20)
Ni2	3	0	0	0	0.017(4)	1.16(20)
Co1	3	0	0	0.5	0.1	0.23(1)
Ni1	3	0	0	0.5	0.783(4)	0.23(1)
Mn1	3	0	0	0.5	0.1	0.23(1)
Li2	3	0	0	0.5	0	0.23(1)
O1	6	0	0	0.23673(6)	1	0.37(1)

Table S20. Structure of 4.6 V charged NCA refined using multiple bank NOMAD data (R_{wp} = 2.00%, gof = 6.03)

S.G. *R*-3m a = 2.80792(5) Å c = 14.1524(4) Å						
Atom	Wyck.	*x*	*y*	*z*	Occ.	B_{eq} (Å^2)
Li1	3	0	0	0	0.183(7)	0.60(16)
Ni2	3	0	0	0	0.008	0.60(16)
Co1	3	0	0	0.5	0.15	0.21(1)

Ni1	3	0	0	0.5	0.792	0.21(1)
Mn1	3	0	0	0.5	0.05	0.21(1)
Li2	3	0	0	0.5	0	0.21(1)
O1	6	0	0	0.23541(4)	1	0.31(1)

Table S21. Analytical conditions for *in situ* gas analysis

Model	: GCMS-QP2020 NX		
Column	: Polymicro glass capillary 1068150019 [45 in. × 75 ± 3 µm I.D. × 363 ± 10 µm O.D.]		
[GC]		[MS]	
Injector Temp.	: N/A	Interface Temp.	: 250 °C
Injection Method	: N/A	Ion Source Temp.	: 200 °C
Split Ratio	: N/A	Ionization Mode	: EI
Carrier Gas	: N/A	Acq. Mode	: Scan
Linear Velocity	: N/A	Scan Range	: m/z 2-100
Column Temp.	: 30 °C	Event Time	: 10 sec
Injection Volume	: N/A		

Equations

$$d_{Li-O} = \sqrt{(\frac{1}{3} - O_z)^2 * c^2 + \frac{a^2}{3}} = c\sqrt{(\frac{1}{3} - O_z)^2 + \frac{1}{3}(\frac{a}{c})^2} \qquad \text{(S1)}$$

$$d_{TM-O} = \sqrt{(O_z - \frac{1}{6})^2 * c^2 + \frac{a^2}{3}} \qquad \text{(S2)}$$

$$d_{interlayer\_O-O} = \sqrt{(O_z - \frac{1}{6})^2 * c^2 + \frac{a^2}{3}} \qquad \text{(S3)}$$

References:

1. Dahn, J., Phase diagram of Li x C 6. *Phys. Rev. B* **1991,** *44* (17), 9170.
2. Ohzuku, T.; Iwakoshi, Y.; Sawai, K., Formation of lithium-graphite intercalation compounds in nonaqueous electrolytes and their application as a negative electrode for a lithium ion (shuttlecock) cell. *J. Electrochem. Soc.* **1993,** *140* (9), 2490.

3. Levi, M.; Levi, E.; Aurbach, D., The mechanism of lithium intercalation in graphite film electrodes in aprotic media. Part 2. Potentiostatic intermittent titration and in situ XRD studies of the solid-state ionic diffusion. *J. Electroanal. Chem.* **1997,** *421* (1-2), 89-97.
4. Laubach, S.; Laubach, S.; Schmidt, P. C.; Ensling, D.; Schmid, S.; Jaegermann, W.; Thißen, A.; Nikolowski, K.; Ehrenberg, H., Changes in the crystal and electronic structure of $LiCoO_2$ and $LiNiO_2$ upon Li intercalation and de-intercalation. *Phys. Chem. Chem. Phys.* **2009,** *11* (17), 3278-3289.
5. Chen, Z.; Zou, H.; Zhu, X.; Zou, J.; Cao, J., First-principle investigation of Jahn–Teller distortion and topological analysis of chemical bonds in $LiNiO_2$. *J. Solid State Chem.* **2011,** *184* (7), 1784-1790.
6. Anisimov, V. I.; Zaanen, J.; Andersen, O. K., Band theory and Mott insulators: Hubbard U instead of Stoner I. *Phys. Rev. B* **1991,** *44* (3), 943.
7. Petit, L.; Stocks, G.; Egami, T.; Szotek, Z.; Temmerman, W., Ground state valency and spin configuration of the Ni ions in nickelates. *Phys. Rev. Lett.* **2006,** *97* (14), 146405.
8. Reynaud, F.; Mertz, D.; Celestini, F.; Debierre, J.-M.; Ghorayeb, A.; Simon, P.; Stepanov, A.; Voiron, J.; Delmas, C., Orbital frustration at the origin of the magnetic behavior in $LiNiO_2$. *Phys. Rev. Lett.* **2001,** *86* (16), 3638.
9. Hirano, A.; Kanno, R.; Kawamoto, Y.; Takeda, Y.; Yamaura, K.; Takano, M.; Ohyama, K.; Ohashi, M.; Yamaguchi, Y., Relationship between non-stoichiometry and physical properties in $LiNiO_2$. *Solid State Ionics* **1995,** *78* (1-2), 123-131.
10. Kalyani, P.; Kalaiselvi, N., Various aspects of $LiNiO_2$ chemistry: A review. *Science and technology of advanced materials* **2005,** *6* (6), 689.
11. Bianchini, M.; Roca-Ayats, M.; Hartmann, P.; Brezesinski, T.; Janek, J., There and back again—the journey of $LiNiO_2$ as a cathode active material. *Angew. Chem. Int. Ed.* **2019,** *58* (31), 10434-10458.
12. Rougier, A.; Delmas, C.; Chadwick, A. V., Non-cooperative Jahn-Teller effect in $LiNiO_2$: an EXAFS study. *Solid State Commun.* **1995,** *94* (2), 123-127.
13. Korotin, D. M.; Novoselov, D.; Anisimov, V., Paraorbital ground state of the trivalent Ni ion in $LiNiO_2$ from DFT+ DMFT calculations. *Phys. Rev. B* **2019,** *99* (4), 045106.
14. Yamaura, K.; Takano, M.; Hirano, A.; Kanno, R., Magnetic Properties of $Li_{1-x}Ni_{1+x}O_2$ ($0 \lesssim x \lesssim 0.08$). *J. Solid State Chem.* **1996,** *127* (1), 109-118.
15. Chung, J.-H.; Proffen, T.; Shamoto, S.; Ghorayeb, A.; Croguennec, L.; Tian, W.; Sales, B. C.; Jin, R.; Mandrus, D.; Egami, T., Local structure of Li Ni O_2 studied by neutron diffraction. *Phys. Rev. B* **2005,** *71* (6), 064410.
16. Chen, H.; Freeman, C. L.; Harding, J. H., Charge disproportionation and Jahn-Teller distortion in $LiNiO_2$ and $NaNiO_2$: A density functional theory study. *Phys. Rev. B* **2011,** *84* (8), 085108.
17. Foyevtsova, K.; Elfimov, I.; Rottler, J.; Sawatzky, G. A., $LiNiO_2$ as a high-entropy charge-and bond-disproportionated glass. *Phys. Rev. B* **2019,** *100* (16), 165104.
18. Molenda, J.; Wilk, P.; Marzec, J., Structural, electrical and electrochemical properties of LiNiO2. *Solid State Ionics* **2002,** *146* (1-2), 73-79.
19. Mansour, A.; Yang, X.; Sun, X.; McBreen, J.; Croguennec, L.; Delmas, C., In Situ X-Ray Absorption Spectroscopy Study of $Li_{(1-z)}Ni_{(1+z)}O_2$ ($z \leq 0.02$) Cathode Material. *J. Electrochem. Soc.* **2000,** *147* (6), 2104.
20. Tsai, Y.; Hwang, B.; Ceder, G.; Sheu, H.; Liu, D.; Lee, J., In-situ X-ray absorption spectroscopic study on variation of electronic transitions and local structure of $LiNi_{1/3}Co_{1/3}Mn_{1/3}O_2$ cathode material during electrochemical cycling. *Chem. Mater.* **2005,** *17* (12), 3191-3199.
21. Yoon, W.-S.; Balasubramanian, M.; Chung, K. Y.; Yang, X.-Q.; McBreen, J.; Grey, C. P.; Fischer, D. A., Investigation of the charge compensation mechanism on the electrochemically Li-Ion deintercalated $Li_{1-x}Co_{1/3}Ni_{1/3}Mn_{1/3}O_2$ electrode system by combination of soft and hard X-ray absorption spectroscopy. *J. Am. Chem. Soc.* **2005,** *127* (49), 17479-17487.
22. Wang, X.; Fan, X.; Yu, X.; Bak, S.; Shadike, Z.; Waluyo, I.; Hunt, A.; Senanayake, S. D.; Li, H.; Chen, L., The Role of Electron Localization in Covalency and Electrochemical Properties of Lithium-Ion Battery Cathode Materials. *Adv. Funct. Mater.* **2020**, 2001633.

23. Chakraborty, A.; Kunnikuruvan, S.; Kumar, S.; Markovsky, B.; Aurbach, D.; Dixit, M.; Major, D. T., Layered Cathode Materials for Lithium-Ion Batteries: Review of Computational Studies on $LiNi_{1-x-y}Co_xMn_yO_2$ and $LiNi_{1-x-y}Co_xAl_yO_2$. *Chem. Mater.* **2020,** *32* (3), 915-952.
24. Lebens-Higgins, Z. W.; Faenza, N. V.; Radin, M. D.; Liu, H.; Sallis, S.; Rana, J.; Vinckeviciute, J.; Reeves, P. J.; Zuba, M. J.; Badway, F., Revisiting the charge compensation mechanisms in $LiNi_{0.8}Co_{0.2-y}Al_yO_2$ systems. *Materials Horizons* **2019,** *6* (10), 2112-2123.
25. Lee, G. H.; Wu, J.; Kim, D.; Cho, K.; Cho, M.; Yang, W.; Kang, Y. M., Reversible Anionic Redox Activities in Conventional $LiNi_{1/3}Co_{1/3}Mn_{1/3}O_2$ Cathodes. *Angew. Chem. Int. Ed.* **2020,** *59* (22), 8681-8688.
26. Aydinol, M.; Kohan, A.; Ceder, G.; Cho, K.; Joannopoulos, J., Ab initio study of lithium intercalation in metal oxides and metal dichalcogenides. *Phys. Rev. B* **1997,** *56* (3), 1354.
27. Zaanen, J.; Sawatzky, G.; Allen, J., Band gaps and electronic structure of transition-metal compounds. *Phys. Rev. Lett.* **1985,** *55* (4), 418.
28. Imada, M.; Fujimori, A.; Tokura, Y., Metal-insulator transitions. *Rev. Mod. Phys.* **1998,** *70* (4), 1039.